

The Redshift Evolution of the High-Mass End of the Red Sequence Luminosity Function from the SDSS-III/BOSS CMASS Sample

Antonio D. Montero-Dorta^{1*}, Adam S. Bolton¹, Joel R. Brownstein¹, Molly Swanson⁵, Kyle Dawson¹, Francisco Prada^{2,3,4}, Daniel Eisenstein⁵, Claudia Maraston⁶, Daniel Thomas⁶, Johan Comparat^{3,4}, Chia-Hsun Chuang^{3,4}, Cameron K. McBride⁵, Ginevra Favole^{3,4}, Hong Guo¹, Sergio Rodríguez^{3,4}, Donald P. Schneider^{7,8}

¹ *Department of Physics and Astronomy, The University of Utah, 115 South 1400 East, Salt Lake City, UT 84112, USA*

² *Instituto de Astrofísica de Andalucía (CSIC), Granada, E-18008, Spain*

³ *Campus of International Excellence UAM+CSIC, Cantoblanco, E-28049 Madrid, Spain*

⁴ *Instituto de Física Teórica, (UAM/CSIC), Universidad Autónoma de Madrid, Cantoblanco, E-28049 Madrid, Spain*

⁵ *Harvard-Smithsonian Center for Astrophysics, 60 Garden St., Cambridge, MA 02138*

⁶ *Institute of Cosmology & Gravitation, University of Portsmouth, Dennis Sciama Building, Portsmouth PO1 3FX, UK*

⁷ *Department of Astronomy and Astrophysics, The Pennsylvania State University, University Park, PA 16802*

⁸ *Institute for Gravitation and the Cosmos, The Pennsylvania State University, University Park, PA 16802*

Accepted —. Received —; in original form —

ABSTRACT

We present the redshift evolution of the high-mass end of the $^{0.55}i$ -band Red Sequence Luminosity Function (RS LF) within the redshift range $0.52 < z < 0.65$, obtained from the DR10 BOSS CMASS sample, which comprises $\sim 600,000$ galaxies. We have developed an analytical method based on an unbinned maximum likelihood approach for deconvolving the observed CMASS distribution from photometric errors and accounting for selection effects. This procedure requires modeling the covariance matrix for the i -band magnitude, $g-r$ color and $r-i$ color using Stripe 82 multi-epoch data. The error-deconvolved intrinsic RS distribution is consistent with a single point in the color-color plane, which implies that the great majority of the observed scatter is due to photometric errors. We estimate that RS completeness is $\sim 0.80 - 0.85$ at $z \geq 0.52$ in the CMASS sample, dropping drastically below that redshift. Approximately 37% of all objects in the CMASS sample belong intrinsically to the blue cloud, which extends to the red side of the color-color diagram. Within the redshift and absolute magnitude range considered ($^{0.55}M_i \lesssim -22$), the evolution of the RS LF is consistent with a Schechter Function of $\Phi_* = (6.693 \pm 0.042) \times 10^{-4} \text{ Mpc}^{-3} \text{ mag}^{-1}$, passively fading at a rate of $1.180 \pm 0.001 \text{ mag}$ per unit redshift. This result implies, assuming a single stellar population (SSP), an age of $\sim 4 - 5 \text{ Gyr}$ at $z = 0.70$, and a formation redshift of $z = 2 - 3$, for the luminous red galaxy (LRG) population (independently of the SSP model used). As for the intrinsic RS colors, the implications of our measurements appears to depend on the stellar population synthesis models that we compare with. FSPS models (Conroy et al. 2009) within a grid covering a wide range of metallicities and dust contents tend to predict a milder evolution as compared to the observations. The best agreement seems to be found for solar-metallicity, dust-free FSPS models with ages greater than $\sim 5 \text{ Gyr}$, which would be consistent with our fading rate results. The Maraston et al. (2009) passive LRG model provides an excellent match to the color-redshift trend, implying an age of $\sim 3 - 4 \text{ Gyr}$ at $z = 0.70$. In the last section we discuss future applications of our results.

Key words: surveys - galaxies: evolution - galaxies: luminosity function, mass function - galaxies: statistics - methods: analytical - methods: statistical

1 INTRODUCTION

In the favored cold dark matter (CMD) cosmological model galaxies grow from primordial fluctuations in a hierarchical fashion, with smaller galaxies merging into larger systems (White & Rees 1978; Blumenthal et al. 1984; White & Frenk 1991). This hierarchical merging is the main mechanism that explains the way galaxies assemble their mass in the Universe. The evolution of the properties of galaxies is, however, driven by the interplay of a number of physical processes, including mergers of a variety of types, accretion, star formation, AGN activity and internal processes such as the evolution of the stellar population (e.g., Kauffmann et al. 1993; Somerville & Primack 1999; Kauffmann et al. 2004; Springel et al. 2005; Croton et al. 2006). The relations between all these processes, their environmental dependencies and their contribution to galaxy evolution across cosmic time, is currently a subject of intense research.

The study of galaxy evolution has benefited remarkably in the last decades from the design and execution of progressively larger and deeper galaxy redshift surveys (e.g., Center for Astrophysics Redshift Survey, CfA, Huchra et al. 1983, Falco et al. 1999; Las Campanas Redshift Survey, LCRS, Shectman et al. 1996; the Two Degree Field Galaxy Redshift Survey, 2dFGRS, Colless et al. 2001; the Sloan Digital Sky Survey, SDSS, York et al. 2000; the DEEP2 Redshift Survey Newman et al. 2013). These large-scale structure surveys have become progressively more specifically designed for a primary scientific goal. One scientific case that has drawn remarkable attention in the last years is the detection of the Baryon Acoustic Oscillation (BAO, Eisenstein et al. 2001) signal imprinted in the large-scale distribution of galaxies; an overdensity of baryonic matter that can be used as a *standard ruler* for measuring the acceleration of the Universe and, consequently, exploring the nature of dark energy (Eisenstein et al. 2001, 2005). The largest of these BAO experiments to date is the Baryon Oscillation Spectroscopic Survey (BOSS, Schlegel et al. 2009, Dawson et al. 2013) of the SDSS-III (Eisenstein et al. 2011). Building on the work of Eisenstein et al. (2001, 2005), BOSS focuses on luminous red galaxies (LRGs) to measure the BAO at $z \simeq 0.55$, providing a sample of over 1.5 million of these type of massive galaxies. This paper takes advantage of a sample of such unprecedented size in order to shed light into the late evolution of the LRG population. The LRG population constitutes the massive end ($M_* \gtrsim 5 \times 10^{10} M_\odot$) of the red sequence luminosity function (RS LF). The red sequence, which is comprised mainly by elliptical galaxies with rather old stellar populations, is considered the last stage in the evolutionary path of most galaxies (e.g., Strateva et al. 2001; Bell et al. 2004)

In this work we model the massive end of the field RS LF using the CMASS galaxy sample, the largest of the BOSS samples. The LF, defined as the intrinsic comoving number density of galaxies per unit absolute magnitude, is a fundamental statistical property of a galaxy population. The shape of the LF, which is commonly parametrized using a Schechter Function (Schechter 1976), contains important information regarding the formation and evolution of a galaxy

population. At low redshift the field LF has been determined from a number of galaxy samples, of varying sizes, photometric depths and selection schemes (e.g., Marzke et al. 1994 with the CfA RS; Lin et al. 1996 with the LCRS; Loveday 1997 with the Stromlo-APM Survey; Blanton et al. 2001, Blanton et al. 2003 and Montero-Dorta & Prada 2009 with SDSS Main Galaxy Sample; Norberg et al. 2002 with the 2dFGRS). At higher redshift, measuring the field LF is challenging because of low number statistics, small survey areas, strong selection effects and large photometric errors. Some notable examples of high-redshift field LF measurements are Wolf et al. (2003) for the Combo-17 survey, Willmer et al. (2006) for the DEEP2 GRS, Faber et al. (2007) for the DEEP2 RS and COMBO-17, Cool et al. (2008) using some extended SDSS data and Maraston et al. (2013) for BOSS.

The redshift evolution of the LF allows a test of an important assumption regarding the massive red sequence population: the passive evolution assumption. A galaxy is said to enter a passive-evolving phase when it does not experience mergers that can alter the fading evolution of its stellar populations. Cool et al. (2008), by computing the LF, found results in agreement with such a hypothesis for the massive ($L > 3L^*$) RS population at $z < 1$. This conclusion was drawn from a combined sample of $\sim 60,000$ LRGs at $0.1 < z < 0.4$ and 300 LRGs at $0.6 < z < 1$. The small size of the high-redshift sample hinders, however, the interpretation of their results. The Cool et al. (2008) results appear to be in agreement with more recent findings by Maraston et al. (2013), who use an extensive sample of $\sim 400,000$ LRGs from BOSS DR9 (Ahn et al. 2012), within the redshift range $0.2 < z < 0.7$. Maraston et al. (2013) computed an observed stellar mass function for BOSS, but no completeness correction was applied. Finally, Tojeiro et al. (2012) present a method for identifying the progenitors of SDSS I/II LRGs within the BOSS sample. They conclude that the LRG population at $z < 0.7$ evolves slowly, i.e., less than 2 per cent by merging, when the two samples are properly matched and weighted.

What appears well established is that the stars in the majority of the low- z , early-type galaxies were formed at $z \gtrsim 2$, with little (or no) indications of star formation occurring since that time. Evidence for this interpretation has been gathered by analyzing the color, luminosity and surface brightness evolution of early-type galaxies in clusters located at $z \lesssim 1$ (Bower et al. 1992, Ellis et al. 1997, Kodama et al. 1998, de Propris et al. 1999, Brough et al. 2002, Holden et al. 2005, Wake et al. 2005). Similar conclusions, regarding the old age of the stars in elliptical galaxies, have been drawn when extending the samples to lower density regions, including the field. A number of recent papers using both spectroscopic and photometric techniques report confirmation the aforementioned ideas (Bernardi et al. 2006, Jimenez et al. 2007 using the SDSS; McCarthy et al. 2004, Glazebrook et al. 2004 using the Gemini Deep Deep Survey (GDDS); Thomas et al. 2005 using a sample of 124 early-type galaxies).

Even though the majority of the early-type galaxy population is quite old, there appears to be a fraction that exhibit clear signs of recent star formation (e.g., Clemens et al.

2009, Schawinski et al. 2007, Balogh et al. 2005). In fact, it has become clear in recent years that star formation in early-type galaxies (and also in late-type galaxies) depends strongly on both stellar mass and the density of the environment. As a matter of fact, indications of star formation are considerably more common among intermediate-to-low mass early-type galaxies and among early-type galaxies residing in lower-density environments. Two notable examples of studies supporting these ideas are Clemens et al. (2006) and Thomas et al. (2010), where large spectroscopic samples of low- z , early-type galaxies extracted from the SDSS are analyzed. Thomas et al. (2010), in particular, infer that intermediate-mass and low-mass galaxies show evidence for a secondary peak of more recent star formation around 2.5 Gyr ago.

The motivation of this paper is twofold: shedding light into the evolution of the LRG population and providing the adequate framework for future galaxy evolution studies using BOSS. The BOSS galaxy selection is performed by applying a rather complicated set of color-magnitude cuts designed to isolate the high-mass end of the red sequence as a function of redshift. In particular, BOSS focuses on the redshift range $0.4 < z < 0.7$, which is considerably higher than the SDSS Main Galaxy Sample range ($z \leq 0.2$, see Strauss et al. 2002). This situation implies lower S/N for the spectra and larger photometric errors that distort the target distribution of magnitudes and colors from which the BOSS samples are collected. Moreover, model magnitudes, from which the colors used in the CMASS selection are built, are known to exhibit correlations between different bands, as the best-fit profile from the r band, convolved with the PSF in each band, is used as a matched aperture for all bands (Strateva et al. 2001; Stoughton et al. 2002). This type of blurring and selection effects are, in fact, common to many ongoing and future large-scale structure surveys (e.g., BOSS; the Extended Baryon Oscillation Spectroscopic Survey, eBOSS; the Dark Energy Spectroscopic Instrument, DESI). The use of large-scale structure surveys as a tool for measuring well-defined cosmological features, such as the BAO, results in survey requirements that are aimed at maximizing the global, statistical efficiency of the survey, at the cost of marginalizing the quality of individual-object measurements. This shift from a traditional object-oriented to a more statistically-oriented survey design should be reflected in the way we analyze the data: *instead of individual galaxy properties our goal is to constrain distributions of galaxy properties*. From the galaxy evolution perspective, the extent to which the BOSS potential can be realized strongly depends on our ability to decouple these effects, by understanding selection effects and being able to deconvolve the observed distributions from photometric uncertainties. In this sense, understanding sample completeness is a condition sine qua non for putting the BOSS datasets into the galaxy evolution context.

This paper is organized as follows. In Section 2 we describe the target selection for the BOSS CMASS sample (2.1) and we discuss the observed CMASS distributions in the color-color-magnitude space (2.2). Section 3 is devoted to describing the procedure for modeling of the covariance

matrix for colors and magnitudes using Stripe 82 multi-epoch data. In Section 4 we discuss the expected shape for the massive end of the intrinsic distribution as predicted by stellar population synthesis models (4.1) and provide some preliminary indications obtained from a simple histogram deconvolution method (4.2). In Section 5 we describe in detail our analytical method for deconvolving the observed CMASS distribution, focusing on the construction of the CMASS probability density distribution (5.1), the computation of the best-fit intrinsic distribution (5.2), the inclusion of physically motivated priors (5.3) and the prescription for correcting for possible inconsistencies in the modeling of the covariance matrix (5.4). In Section 6 we present the main results of this paper, including: the best-fit intrinsic distribution at $z = 0.55$ (6.1), the redshift evolution of best-fit parameters (6.2), the RS completeness in the CMASS sample (6.3) and the evolution of the massive-end of the RS LF. We also discuss in this section the fading rate of the high-mass end of the RS LF (6.5) and the color evolution of the RS (6.6). Finally, in Section 7 we summarize the main conclusions of this study and discuss future applications of our results. Throughout this paper we adopt a cosmology with $\Omega_M = 0.274$, $\Omega_\Lambda = 0.726$ and $H_0 = 100h$ km s $^{-1}$ Mpc $^{-1}$ with $h = 0.70$ (WMAP7, Komatsu et al. 2011), and use AB magnitudes (Oke & Gunn 1983).

2 THE BOSS CMASS SAMPLE

In this paper we make use of spectroscopic and photometric data from the Tenth Data Release of the SDSS (DR10, Ahn et al. 2013). The SDSS DR10 is the third release within the SDSS-III, and the second release where BOSS data is included. The spectroscopic DR10 BOSS sample comprises a total of 927,844 galaxy spectra and 535,995 quasar spectra (an increase of almost a factor two as compared to the SDSS DR9, Ahn et al. 2012). The baseline imaging sample for the BOSS spectroscopic survey is the final SDSS imaging data set, which was released as part of the DR8 (Aihara et al. 2011), and contains both the SDSS-I and II imaging data. These imaging programs provide five-band *ugriz* imaging over 7600 sq deg in the northern Galactic hemisphere and ~ 3100 sq deg in the southern Galactic hemisphere, with a typical 50% completeness limit for detection of point sources at $r = 22.5$. Refer to the following references for technical information about the SDSS survey: Fukugita et al. (1996) for a description of the SDSS *ugriz* photometric system; Gunn et al. (1998) and Gunn et al. (2006) for technical aspects of the SDSS camera and the SDSS telescope, respectively; Smee et al. (2013) for information about the SDSS/BOSS spectrographs.

The catalog that we use to compute the RS LF is the DR10 Large Scale Structure catalog (DR10 LSS). This catalog, which is thoroughly described in Anderson et al. (2014), incorporates a detailed treatment of angular incompleteness (caused by fiber collisions and redshift failures) and of a variety of systematics that could potentially affect the target density of spectroscopically identified galaxies (e.g. stellar density, seeing, Galactic extinction, etcetera). The DR10

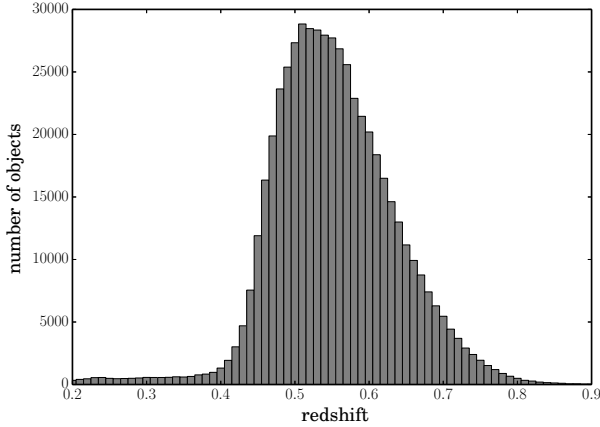


Figure 1. Redshift distribution for the entire CMASS sample in bins of $\Delta z = 0.01$. The total number of unique CMASS galaxies with a good redshift estimate and with model and cmodel apparent magnitudes and photometric errors in all g,r and i bands is 549,005.

LSS catalog includes galaxies from the SDSS Legacy Survey, which basically contains the SDSS-I survey and a small fraction of the SDSS-II survey. We refer to Anderson et al. (2014) for further details about this catalog. In the remainder of this section we focus on summarizing the main steps involved in the selection of the BOSS galaxy target sample, and, in particular, of the CMASS sample that we use in this work.

The BOSS galaxy target sample is built from the SDSS imaging footprint in two steps. Firstly, an imaging pre-selection is performed to ensure that only detections passing a particular set of quality criteria are chosen as targets. Subsequently, a set of color-magnitude cuts is applied to the resulting catalog to select the LRG sample required to effectively measure the BAO. We focus here on this second step; and we refer to Dawson et al. (2013) for a detailed description of the SDSS imaging pre-selection (see Section 2.2 in the aforementioned paper). Further technical details about this process can also be found in Stoughton et al. (2002), Richards et al. (2006), and the SDSS-III Web site.¹

2.1 The CMASS galaxy target selection

The BOSS galaxy target selection is based on a similar strategy as that used by Eisenstein et al. (2001) to build the SDSS I-II LRG sample. In essence, the selection was designed to produce two different galaxy samples: a low-redshift sample called *LOWZ* and a high-redshift sample called *CMASS*. The *LOWZ* sample contains LRGs within the redshift range $0.15 < z < 0.43$. The *CMASS* sample, which is the one that we use in this study, covers a nominal redshift range $0.43 < z < 0.70$, although it extends slightly beyond these limits. The word CMASS stands for "constant mass", emphasizing the fact that the sample was designed to be ap-

proximately stellar mass-limited. This requisite naturally introduces a highly incomplete population of green valley and blue cloud galaxies that increases with redshift.

The CMASS selection scheme consists of the following magnitude, color and color-magnitude cuts:

$$\begin{aligned}
 17.5 < i_{cmod} < 19.9, \\
 r_{mod} - i_{mod} < 2, \\
 i_{fiber2} < 21.5, \\
 d_{\perp} > 0.55, \\
 i_{cmod} < 19.86 + 1.6 \times (d_{\perp} - 0.8)
 \end{aligned} \tag{1}$$

where $d_{\perp} = (r_{mod} - i_{mod}) - (g_{mod} - r_{mod})/8$ and i_{fiber2} is an i-band magnitude within a 2-arcsec diameter aperture. The subscript *mod* and *cmod* denote model and cmodel magnitudes, respectively. Model magnitudes are more efficient at tracing galaxy colors, whereas the cmodel i-band flux is the best proxy for the galaxy flux. All colors quoted in this paper are *model* colors and all magnitudes *cmodel* magnitudes, unless otherwise stated (hereafter we drop the subindices when we refer to these quantities). For more information on the BOSS selection refer to Eisenstein et al. (2011) and Dawson et al. (2013).

The spectroscopic CMASS sample is obtained from the CMASS galaxy target sample, which results from the application of both the imaging pre-selection and the CMASS cuts described above to the SDSS DR8 imaging data set. This process, as it is discussed in detail in Anderson et al. (2014), is known to suffer from some degree of incompleteness, that mainly manifests itself in two forms. Because of the finite size of the fiber plugs in the spectrographs, two spectroscopic fibers cannot be located simultaneously at any distance closer than 55 arcsec. This is the well-known *fiber collision* problem, which affects almost uniformly the SDSS footprint and is the source of some 6% of all incompleteness in the survey (Blanton et al. 2003). This form of incompleteness occurs during the tiling process, when fibers are assigned to targets. Additionally, even if a fiber is already assigned to an object, there is a probability that the BOSS automated redshift determination pipeline fails to provide a redshift estimation with the required accuracy. A detailed description of the automated spectral classification, redshift determination, and parameter measurement pipeline in use for BOSS, as of DR9, is presented in Bolton et al. (2012). Within the CMASS sample, at redshift $0.4 \leq z \leq 0.8$, the pipeline achieves an automated classification success rate of 98.70% and confirms 95.4% of unique CMASS targets as galaxies (from all galaxies actually entering the pipeline). Note that the difference between these percentages arises from stars that pass the CMASS selection criteria.

Redshift failures and fiber collisions should have little correlation with color or magnitude. Under this assumption, this type of incompleteness simply translates into some small uncertainty in the determination of the normalization of the luminosity function. However, the presence of large photometric errors implies that legitimate CMASS galaxies can

¹ <https://www.sdss3.org>

scatter outside our selection boundaries, and, conversely, non-CMASS galaxies can contaminate our sample. Understanding this effect in the BOSS CMASS sample is one of the main goals of this work.

In Figure 1 we show the redshift distribution for the CMASS spectroscopic sample in bins of $\Delta z = 0.01$. This is the redshift bin size that we use throughout this paper. The total number of unique CMASS galaxies with a good redshift estimate and with model and *cmodel* apparent magnitudes and photometric errors in all *g*, *r* and *i* bands is 549,005. The mean value of the redshift distribution in Figure 1 is 0.532 and its standard deviation 0.128; approximately $\sim 7.5\%$ and $\sim 4.5\%$ of galaxies lie below and above the nominal low redshift and high redshift limits, i.e., $z = 0.43$ and $z = 0.70$, respectively.

2.2 CMASS observed distributions in color-color-magnitude space

As described in Section 2.1, the main quantities involved in the CMASS selection are the *g-r* and *r-i* colors, and the *i*-band apparent magnitude. We assume here that completeness in the CMASS sample depends only on this small set of quantities. Let this set form a 3D space such that the first axis is *i*, the second axis is the *g-r* color and the third axis is the *r-i* color. We denote these coordinates as *X*, *Y*, *Z*. In any given redshift slice (of size $\Delta z = 0.01$) we bin the CMASS data within this 3D space, using a constant bin size of $\Delta X = 0.1$, $\Delta Y = 0.1$ and $\Delta Z = 0.1$.

Figure 2 presents in a *g-r* vs. *r-i* color-color diagram the distribution of CMASS galaxies in a redshift slice centered at $z = 0.55$ ($\Delta z = 0.01$), for different apparent magnitude bins. The $z = 0.55$ bin is very close to the mean redshift of the CMASS sample (Figure 1). Figure 2 illustrates the type of broadened color-color distributions that we find in the BOSS galaxy data. The red sequence appears as an irregular blob, elongated mostly in the *g-r* direction, that is progressively more populated towards the fainter magnitude bins. Adjacent to the red sequence, in the *g-i* direction (diagonal in this diagram), is a population of bluer galaxies, which are not excluded by the CMASS selection. At $z = 0.55$, these objects correspond, at least in observed space, to the upper, redder part of the blue cloud and to the so-called green valley, the narrow region between the blue cloud and the red sequence.

The observed CMASS distribution is strongly affected by the d_{\perp} constraint (solid line in Figure 2), that was designed to lie parallel to the locus of a passive evolving population of galaxies. This cut isolates the red sequence, while allowing for a population of bluer galaxies. In practice, the d_{\perp} demarcation is not fixed, but actually depends on magnitude. It is determined by the combination of the d_{\perp} cut and the d_{\perp} - *i*-band magnitude cut (dashed line in Figure 2). Rearranging in Equation 2, the d_{\perp} demarcation at a given apparent magnitude, *i*, is given by the following 2 inequations:

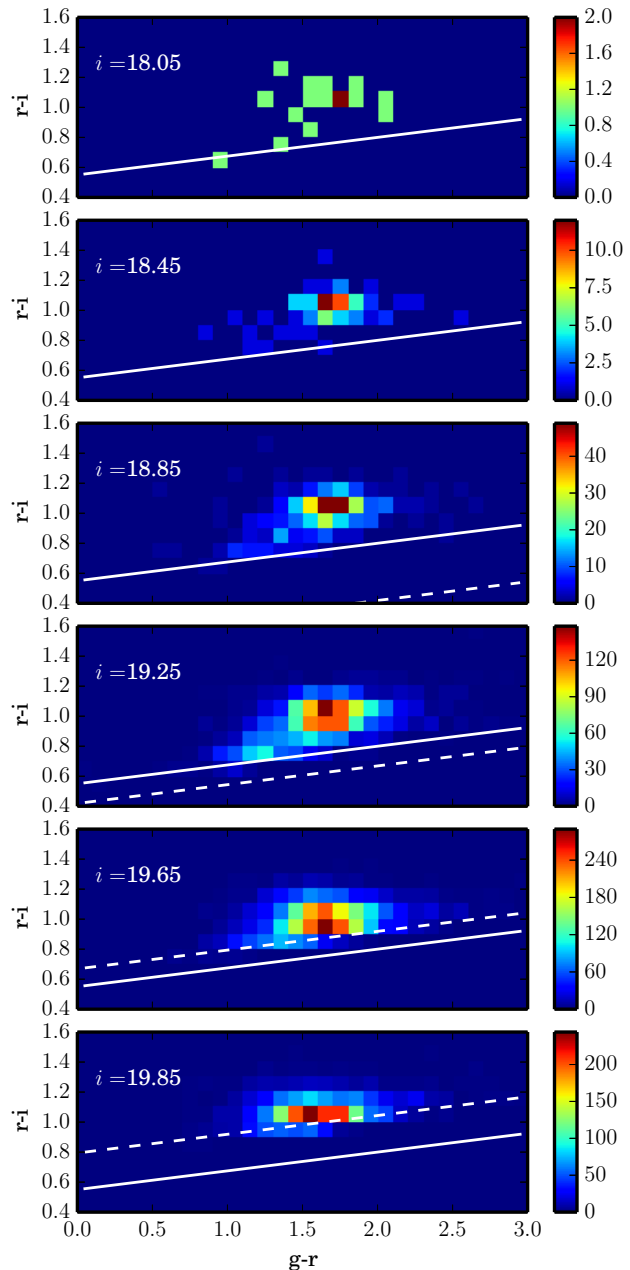


Figure 2. Distribution of CMASS galaxies in a *g-r* vs. *r-i* color-color diagram for a redshift bin centered at $z = 0.55$, with a width of $\Delta z = 0.01$. In each panel, the solid and dashed lines represent the d_{\perp} demarcation $d_{\perp} > 0.55$, and the sliding cut $i < 19.86 + 1.6 \times (d_{\perp} - 0.8)$, respectively. The observed CMASS distributions are considerably blurred by photometric errors, especially along the *g-r* axis. The typical photometric error quoted in the catalog is ~ 0.20 for the *g-r* color and ~ 0.08 for the *r-i* color. Determining the error-deconvolved intrinsic color-color-magnitude distribution is a key step in the computation of the RS LF.

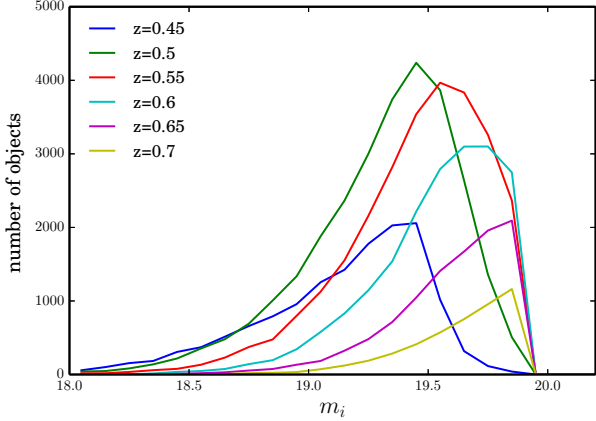


Figure 3. CMASS number counts for different redshift slices, from $z = 0.45$ to $z = 0.70$. CMASS number counts are strongly affected by selection effects and photometric errors. By determining the intrinsic number counts we can correct for this incompleteness.

$$d_{\perp} > 0.55, \\ d_{\perp} > 0.8 + \frac{i - 19.86}{1.6} \quad (2)$$

which implies that the d_{\perp} condition starts to be more restrictive at $i > 19.46$. It is also quite evident from Figure 2 that the $r - i < 2$ cut has little impact on the CMASS distribution.

The CMASS color-color diagram changes remarkably when we examine different redshift slices, due to a combination of intrinsic evolution and the effect of redshift itself. In terms of the CMASS selection, the fraction of the red sequence and the blue cloud accessible increases with redshift. At $z \simeq 0.45$, only the top of the red sequence is targeted, whereas at $z \simeq 0.65$ both the red sequence and the blue cloud are fairly well represented (even though the effective magnitude range shrinks remarkably).

In Figure 3 we show the CMASS number counts, i.e. the distribution of CMASS galaxies in bins of i -band magnitude, for six different redshift slices, from $z = 0.45$ to $z = 0.70$. The shape of the number counts in Figure 3 is determined by several factors, including, of course, redshift. First of all, it is the expected passive evolution of the LRG population. Secondly, number counts are affected by selection effects, which are responsible for the drop of the number of objects at the faint end. The third element is represented by the covariance matrix. Photometric errors scatter objects around in the 3D space, including along the i -band axis. These errors and the covariances between different bands are larger in the $g - r$ vs. $r - i$ plane than along the i -band axis, so their impact is more noticeable on the distribution of colors shown in Figure 2 than on the number counts of Figure 3.

3 STRIPE 82 DATA: MODELING THE COVARIANCE MATRIX

In order to model the blurring effect produced by photometric errors and correlations between different $ugriz$ bands, we use Stripe 82 multi-epoch data. Stripe 82 is the SDSS stripe along the celestial equator in the southern Galactic cap. An SDSS *stripe* is a region along a great circle in the sky with a constant width of 2.5 deg, defined by the projected angular size of the SDSS camera. Each stripe is surveyed by at least two *runs*, which are continuous scans of the imaging telescope. The focal plane of the survey camera has six columns of CCDs, so that a single run consists of six camera columns or *camcols*. Camcols are separated by a gap that can only be filled by an offset second run. Each of the two interleaving runs covering a stripe are called *strips*, and denoted by the letters N (north) and S (south), respectively. The Stripe 82 is, therefore, 2.5 deg wide, and covers the region defined by $-50^{\circ} < \alpha_{J2000} < 59^{\circ}$; $-1.25^{\circ} < \delta_{J2000} < 1.25^{\circ}$, i.e. a total of ~ 270 sq deg in the sky.

What makes Stripe 82 especial and particularly useful for this work is the fact that it was observed multiple times. In fact, it was observed as many as ~ 80 times before the final release of the Stripe 82 database (usually as part of the SDSS-II supernova survey, Frieman et al. 2008), as part of the SDSS DR7 (Abazajian et al. 2009). The Stripe 82 database is comprised by a total of 303 runs, plus two coadd runs. These runs correspond to different *reruns*, which is how the processing algorithm used is indicated. In different reruns, the underlying imaging data is the same, but the software version and/or calibration are different. By imposing the latest Stripe 82 rerun, our Stripe 82 database is reduced to 120 runs. To this subset, we add 30 extra runs which are not included in the official Stripe 82 database but have some overlap with the Stripe 82 region, thus we have a total of 150 runs.

The total number of detections, of any type, in this data base exceeds 100 millions, including galaxies, stars, transients of all kinds, artefacts and of course multiple observations of the same object. Our goal is to generate a Stripe 82 multi-epoch galaxy catalog that is, on average, unbiased with respect to the SDSS imaging catalog from which the BOSS target galaxy sample was selected. There is an implicit assumption here that the photometric quality of the Stripe 82 data and that of the SDSS footprint are comparable. As we discuss below, an inconsistency here would be likely to either lead to an erroneous solution for the intrinsic distribution or hinder the convergence of our deconvolution algorithm. We therefore need to incorporate some flexibility in the modeling, so that it can accommodate possible global inconsistencies.

Each run in the database (and in the SDSS in general) is divided into a number of *fields*, this number varying for different runs. For each field, all the needed individual-detection photometric information is contained in the *PhotoObj* files. Geometric and general photometric information for the corresponding field and run are stored in the upper-level *PhotoField* and *PhotoRun* files, respectively. A number of fields from different runs overlap in our Stripe 82

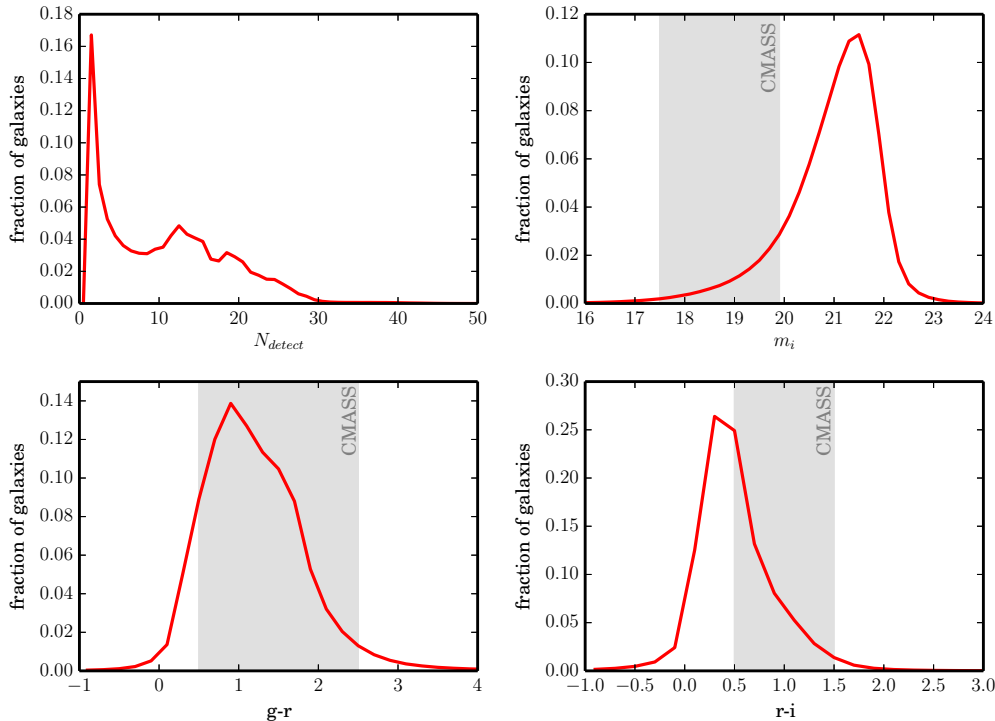


Figure 4. The distribution of the number of detections (N_{detect}), the i-band magnitude, the g-r color and the r-i color for the entire multi-epoch Stripe 82 summary catalog. In the last three panels, a shaded region highlights the approximate range covered by the CMASS sample. We use this catalog to model the covariance matrix of magnitudes and colors for the BOSS data. This error model is a fundamental ingredient of our deconvolution procedure.

database, thus giving rise to multiple observations for the same object. In order to identify unique objects within the data base, we use the identification number `THING_ID`, which is the same for all detections of the same object across different runs.

The `THING_ID` identification number allows us to collect all detections for the same object, but the information about how each detection is resolved in the survey is stored in a bitmask called `RESOLVE_STATUS`. Only objects with the `SURVEY_PRIMARY` bit of the `RESOLVE_STATUS` flag set are used for the galaxy targeting algorithms. In order to collect a set of detections for each unique object, we must replace this condition. Thus, we require all detections to have the `RUN_PRIMARY` bit set. This criterion guarantees that detections are unique within each run. In essence, the `RUN_PRIMARY` bit resolves duplicates along the edges in the drift scan direction in the overlap region between adjacent fields in the same run.

Finally, we require that all detections pass the SDSS photometric pre-selection criteria (Dawson et al. 2013, Section 2.2), including the photometric flag cuts and the star/galaxy separation. Note that the `CALIB_STATUS` bitmask allows us to exclude all detections observed in non-photometric conditions, i.e., detections in fields that fail to satisfy the high photometric quality of the survey. This condition, along with the rest of the flag cuts, allow a selection of a multi-epoch sample that should be photometri-

cally comparable with the BOSS imaging footprint. Our final Stripe 82 multi-epoch summary catalog contains a total of 5,173,086 objects that were ever selected (in any epoch) as candidate galaxy targets. Each object has an average of ~ 10 associated detections. For each object in the catalog, we compute the average i-band magnitude, g-r color and r-i color within the corresponding set of detections. We also calculate for each object the standard deviations of each variable (σ_{11} , σ_{22} , σ_{33} for i-band magnitude, g-r color and r-i color, respectively) and the correlations for the cross terms (ρ_{12} , ρ_{13} , ρ_{23}). These elements are all that is needed to compute the covariance matrix for each individual object.

In Figure 4 we present some statistical properties of our Stripe 82 multi-epoch catalog, including the distribution of number of detections (N_{detect}), i-band magnitude, g-r color and r-i color. There is a large fraction of objects for which we only have one or two detections ($\sim 20\%$). These objects are excluded from our analysis, as we set a number of detections threshold at $N_{detect} = 5$ for the computation of individual statistics. In the rest of the panels, shaded regions display the approximate range covered by the CMASS selection.

The covariance matrix shows some non-negligible dependence on magnitude and colors. In order to model this dependence, we first split our Stripe 82 sample in 3D bins of magnitude, g-r color and r-i color, with a constant bin size of $\Delta X = 0.1$, $\Delta Y = 0.1$ and $\Delta Z = 0.1$. In each 3D bin, we compute the median of magnitude, colors, standard

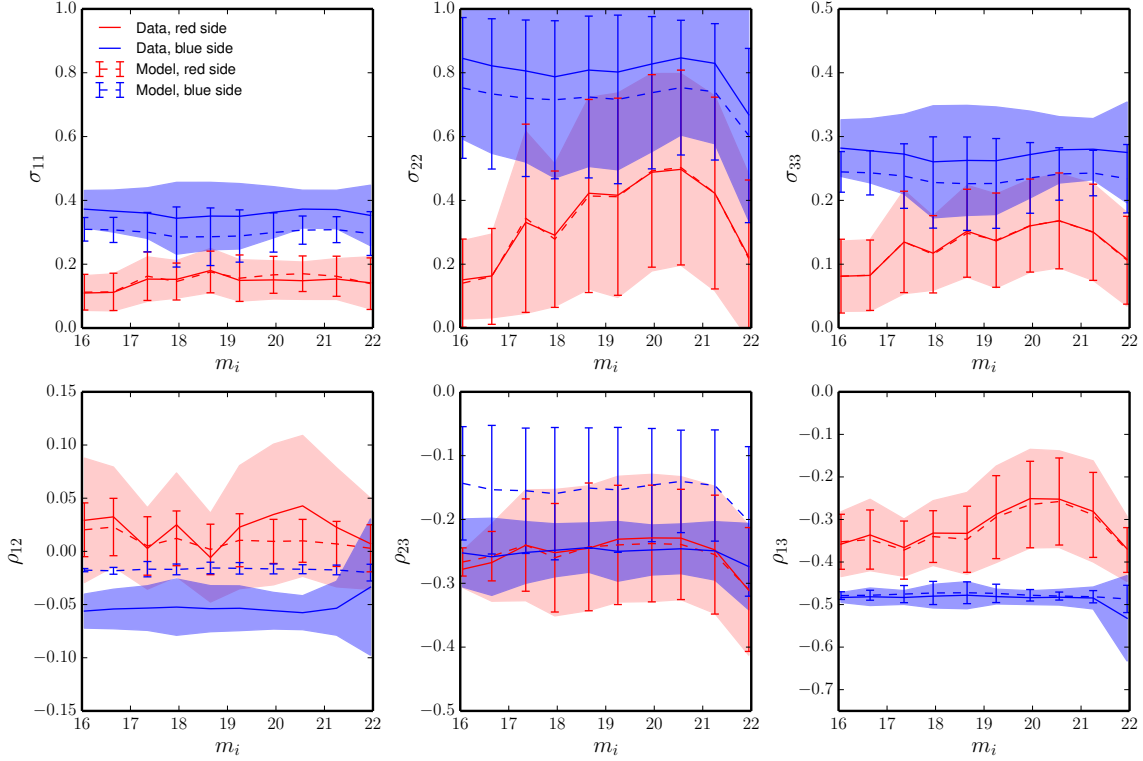


Figure 5. Performance of the best-fit quadratic model for the dependence of the σ_{11} , σ_{22} , σ_{33} , ρ_{12} , ρ_{13} and ρ_{23} terms on color and magnitude. In each panel, the red solid line and the red dashed line represent the average of the corresponding term in bins where $g - i \geq 2.35$ in the data and in the model, respectively. The shaded red region represents the $2\text{-}\sigma$ scatter for the data, and the red error bars the corresponding $2\text{-}\sigma$ scatter for the model. In a similar format but in blue colors we show the average of each term for bins that satisfy $g - i < 2.35$. A visual inspection of the fits reveals that the quadratic model for the σ and the correlation terms is capable of reproducing the general trends reasonably well. This analytical error model is a fundamental ingredient of our deconvolution procedure.

deviation terms and correlation terms, as long as the bin contains at least 25 galaxies. Finally, we assume a quadratic dependence on magnitude and colors for each of the three standard deviation terms and three correlation terms. As an example, the σ_{11} term is modeled as follows:

$$\sigma_{11}(X, Y, Z) = c_{XX}^{11}X^2 + c_{YY}^{11}Y^2 + c_{ZZ}^{11}Z^2 + c_{XY}^{11}XY + c_{YZ}^{11}YZ + c_{XZ}^{11}XZ + c_X^{11}X + c_Y^{11}Y + c_Z^{11}Z + c_0 \quad (3)$$

with 9 different coefficients. Each of the six individual fits is performed only within the region defined by the following ranges: $16 < i < 22$, $0 < g - r < 3$ and $0 < r - i < 1.5$, which exceeds the CMASS selection region.

In Table 1 we provide the average value and the standard deviation for the six different statistics that we model. As expected, the photometric errors on $g-r$ are considerably larger than the photometric errors on the i -band magnitude and $r-i$. This effect is noticeable in Figure 2, as the scatter in the observed CMASS distributions is larger along the $g-r$ axis. Obviously, no correlation exists between the i -band magnitude and the $g-r$ color, and a negative correlation is present between the i -band magnitude and the $r-i$ color and between the $g-r$ color and the $r-i$ color.

element	$\langle \text{element} \rangle$	$\sigma(\text{element})$
σ_{11}	+0.166	0.075
σ_{22}	+0.357	0.301
σ_{33}	+0.138	0.075
ρ_{12}	+0.006	0.048
ρ_{13}	-0.266	0.103
ρ_{23}	-0.335	0.113

Table 1. The mean value and standard deviation for the six different statistical quantities for which we model the color and magnitude dependence (the standard deviation terms σ_{11} , σ_{22} , σ_{33} and the correlation terms ρ_{12} , ρ_{13} , ρ_{23}).

A visual inspection of the fits reveals that the quadratic model is capable of reproducing the general trends reasonably well. In an attempt to illustrate this we present, in Figure 5, the dependence of each term on apparent magnitude, for two different sub-samples, defined by a color demarcation at $g - i = 2.35$. The red solid line and the red dashed line in each panel represent the mean value of the corresponding statistic in bins where $g - i \geq 2.35$ in the data and the model, respectively. The shaded red region repre-

sents the $2\text{-}\sigma$ scatter for the data, and the red error bars the corresponding $2\text{-}\sigma$ scatter for the model. Similarly in blue colors we show the mean value of each term for bins that satisfy that $g - i < 2.35$. The general conclusion is that the best-fit quadratic model reproduces the average magnitude dependencies quite accurately at the red side of the color-color plane (at least up to $g - i \simeq 2$), but some discrepancies appear at the blue side. These discrepancies are consistent with the typical scatter in these relations.

Finally, we must account for possible overall inconsistencies in the photometric quality between the Stripe 82 and the SDSS footprint. To this purpose, we allow our covariance matrix to be multiplied by a scale factor that could in principle have a small dependence on magnitude but should be close to 1. The value or functional form for this factor, that we call $\beta(i)$, will be empirically determined as part of the modeling of the intrinsic distributions.

4 THE EXPECTED SHAPE OF THE INTRINSIC COLOR-COLOR-MAGNITUDE DISTRIBUTION

4.1 Predictions from stellar population synthesis models

Stellar population synthesis (SPS) models are widely used as a tool for interpreting the integrated light from galaxies. In their simplest form (the so-called single stellar populations or SSPs), they model the evolution of a coeval set of stars. More realistic models (composite stellar populations or CSPs) allow for star formation to occur during the lifespan of the galaxy (in a continuous way, in bursts or in a combination of both). Although SPS models are known to suffer from major uncertainties (see Conroy et al. 2009 for a detailed study on SPS uncertainties) it is useful to see how they distribute in a $g\text{-}r$ vs. $r\text{-}i$ color-color diagram within the CMASS redshift range. These models provide a sense of the shape and typical scatter of the intrinsic distribution.

In order to explore the predictions from SPS models, we use the Granada FSPS galaxy product (Montero-Dorta et al., in preparation) based on the publicly available ‘‘Flexible Stellar Population Synthesis’’ code of Conroy et al. (2009). The Granada FSPS product, which is part of the SDSS DR10 (Ahn et al. 2013), provides spectro-photometric stellar masses, ages, specific star formation rates, and other stellar population properties, along with corresponding errors, for the entire DR10 galaxy sample. Here we use the same grid of CSP models with varying star formation history (based on simple τ -models), metallicity and dust attenuation used to generate the Granada FSPS product. This extensive grid of 84,000 models (in its complete version, before applying any priors) was designed to adequately cover the CMASS parameter space.

Figure 6 displays, in white contours, the distribution of FSPS models in a $g\text{-}r$ vs. $r\text{-}i$ color-color diagram, for six redshift slices from $z = 0.45$ to $z = 0.70$. The only prior imposed here is that the look-back formation time of the galaxy cannot exceed the age of the Universe at the corresponding redshift. As mentioned above, models expand a wide range of

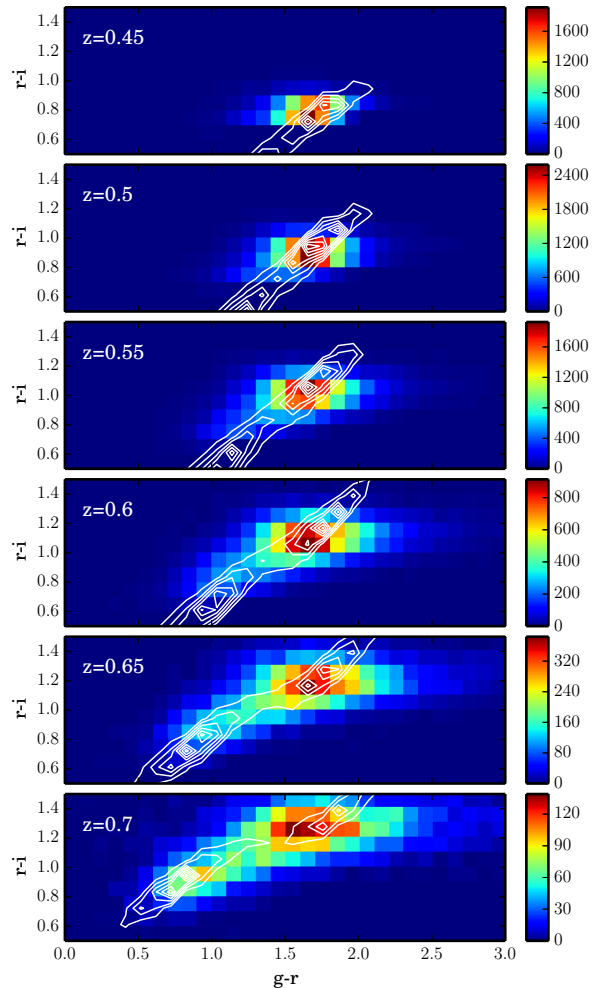


Figure 6. The distribution of FSPS models (white contours) in a $g\text{-}r$ vs. $r\text{-}i$ color-color diagram, for six different redshift slices from $z = 0.45$ to $z = 0.70$. FSPS models are taken from the Granada FSPS galaxy product, which is part of the SDSS DR10 (Ahn et al. 2013). These FSPS models cover a wide range of metallicities, SFHs and dust attenuation levels. The color map shows the distribution of CMASS galaxies in the corresponding redshift slice. The typical photometric error quoted in the catalog is ~ 0.20 for the $g\text{-}r$ color and ~ 0.08 for the $r\text{-}i$ color.

stellar population properties, so the width of the model distribution should be considered an upper-limit prediction for the intrinsic distribution. In the background of each panel, we show the distribution of CMASS galaxies in the corresponding redshift slice. The FSPS models align extremely well with the data at every redshift. As expected, models predict a narrow intrinsic distribution in color space, which suggests that the observed CMASS distribution is remarkably broadened by photometric errors. Interestingly, color bimodality appears naturally in the grid. In addition, the red sequence and the blue cloud form a continuous sequence at redshifts $z \lesssim 0.55$ in the models. This sequence clearly breaks at $z \gtrsim 0.60$, so that both components are no longer

aligned. Again, it is important to note that these model distributions have not been calibrated with observations.

In following sections we discuss how our results compare with the predictions from the FSPS models of Figure 6.

4.2 Lessons from a simple histogram deconvolution approach

Given the expected shape of the intrinsic galaxy distribution, a direct deconvolution of the observed histograms is rather complicated. In essence, the distributions are expected to be so concentrated in the color-color plane that binning effects can be important. The risk is that these effects propagate into the computation of the luminosity function. A simple binned-data approach like this can, however, provide some valuable information about the most probable shape of the intrinsic distributions.

The mapping between the intrinsic and the observed distributions can be performed by applying the CMASS selection mask and a convolution matrix. This convolution matrix must account for the deformation of the intrinsic histogram due to photometric errors, and can be derived from the covariance matrix model (which provides probability that a galaxy in a given bin is scattered into any other bin within our 3D space). By modeling the RS and BC distributions separately, using two Gaussians with parametrized shape and position on the color-color plane, we can reproduce to reasonable accuracy the observed CMASS distributions. In this model, a Schechter function in apparent magnitude units is assumed for the magnitude-dependent amplitude of each Gaussian. Interestingly, in order for the algorithm to converge, it is necessary to reduce the effect of the covariance matrix by $\sim 8\%$ (i.e. $\beta = 0.92$). This deviation might reflect some global differences in the data quality between the Stripe 82 and the BOSS footprint. As expected from the FSPS models of Figure 6, the intrinsic model obtained from a histogram deconvolution method presents the following general characteristics:

- Both the BC and the RS intrinsic distributions are extremely tight, with characteristic σ equal or below our resolution limit of 0.1, especially the RS component.
- The BC component is narrow but also elongated in color-color space. For the RS component, the ellipticity parameter is smaller than 1. Because of the small σ , this value is basically a nuisance parameter in the fitting.
- The model requires a declining magnitude dependence of the centroids of the distributions to provide a good fit for the data. Such a dependence is relevant only in the r-i direction (considering the size of our color bins).
- The inclination of the RS with respect to the g-r axis appears to be greater for the RS than for the BC component.

Tests made by reducing the size of our color bins reveal that the best-fit σ of the RS distribution tend to be proportional to the bin size, indicating that the real width is extremely small, virtually consistent with a single point in the color-color plane. This result implies that basically all the scatter observed for the RS sequence is due to photometric blurring. Reducing the bin size not only fails to solve

the problem, but it also slows down considerably the convergence of the algorithm. We have also checked that setting the RS σ to either a marginally small value or to 0.1, our fiducial bin size, leads to poor fits.

Working below the resolution limit poses the question of whether some of the fitting parameters, such as σ , the ellipticity or the position angle, are actually well constrained. In this context they should simply be considered nuisance parameters. This situation seems risky when computing the intrinsic number counts, and, consequently, the normalization of the luminosity function. These uncertainties prevent us from using a histogram deconvolution method to model the CMASS luminosity function. Instead, in the following section, we describe an analytical method based on an unbinned maximum likelihood approach, that has proven more adequate for the purpose of this work, given the properties of the BOSS data and the intrinsic shape of the galaxy color distribution.

5 ANALYTICAL DECONVOLUTION

Deconvolution procedures based on binned data (histograms) can provide some advantages regarding the convergence of the algorithm and the computation time. However, these methods also suffer from information loss, due to the arbitrariness of the binning process. This aspect is especially relevant in cases where the data is sparse or somehow insufficient.

In this section we describe a deconvolution procedure for the CMASS observed distributions based on an unbinned maximum likelihood method (UML). The key idea here is that the underlying statistical quantity that we optimize, the likelihood \mathcal{L} (or $\log\mathcal{L}$), does not require any artificial binning beyond the one produced by the measurement instruments.

The UML method is based on constructing the predicted probability density function (PDF) for the data as a function of the parameters of interest. Once we have an analytical parametric expression for this PDF, the likelihood of a particular set of values for the parameters, θ , given the data, \vec{d} , can be obtained trivially. This likelihood is equal to the probability, P , of measuring the data given that set of values, which is equal to the product of all individual probabilities, p_i . Namely:

$$\mathcal{L}(\theta|\{\vec{d}\}) = P(\{\vec{d}\}|\theta) = \prod_i p_i(\{\vec{d}_i\}|\theta) \quad (4)$$

To find the best-fit parameters it is common to optimize the logarithm of the likelihood, $\log\mathcal{L}(\theta|\{\vec{d}\})$, instead of the likelihood itself.

The observed PDF for the distribution of CMASS objects in the color-color-magnitude space is shaped by contributions from the intrinsic distribution, the blurring effect of photometric errors and the CMASS selection. For the sake of simplicity we will first restrict the analysis to the red sequence. As we have seen previously, the red sequence can be described with sufficient accuracy in observed space by

PDF parameter	Description
m_*	Characteristic apparent magnitude for intrinsic number counts
α	Faint-end slope of the LF
Y_0	Zero point for the linear dependence of the (g-r) component of the centroid with magnitude
Y_1	Slope for the linear dependence of the (g-r) component of the centroid with magnitude
Z_0	Zero point for the linear dependence of the (r-i) component of the centroid with magnitude
Z_1	Slope for the linear dependence of the (r-i) component of the centroid with magnitude
σ	Intrinsic scatter on the color-color plane
θ	Position angle of the Gaussian Function on the color-color plane w.r.t. the g-r axis
q	Inverse of the ellipticity of the Gaussian Function on the color-color plane
f_{blue}	Observed fraction of blue objects in the CMASS sample
β	Error scale factor for the covariance matrix model

Table 2. Fitting parameters of the PDF for each Gaussian function (m_* , α , Y_0 , Y_1 , Z_0 , Z_1 , σ , θ , q) along with f_{blue} and β

a Gaussian function representing the color-color component and a Schechter function in apparent magnitude accounting for the i-band magnitude dependence. This information is incorporated in our analytical modeling of the PDF.

5.1 The CMASS probability density distribution

In order to build the observed CMASS PDF, we start by expanding the Schechter function (that accounts for the intrinsic number counts) in terms of a non-negative sequence of Gaussians along the i-band magnitude axis:

$$n_{sch}(X, \{\tilde{\phi}_*, m_*, \alpha\}) = \sum_j c_j \mathcal{G}_j \quad (5)$$

where n_{sch} represents the intrinsic number counts (i.e., the intrinsic number of objects at each magnitude bin), $\{\tilde{\phi}_*, m_*, \alpha\}$ are the apparent-magnitude counterparts of the Schechter LF parameters, c_j is coefficient j of the expansion and \mathcal{G}_j is the corresponding Gaussian function. The Schechter Function can be expressed as:

$$n_{sch}(X, \{\tilde{\phi}_*, m_*, \alpha\}) = 0.4 \log(10) \tilde{\phi}_* \left[10^{0.4(m_* - X)(\alpha + 1)} \right] \times \exp\left(-10^{0.4(m_* - X)}\right) \quad (6)$$

Here, we assume that $\alpha = -1$ and $\tilde{\phi}_* = 1$ object, for the sake of simplicity. The magnitude interval considered is $17 < X < 20.5$, which exceeds by half a magnitude the CMASS limits at both ends, in order to avoid boundary problems. For convenience, we choose to use 22 Gaussian functions to completely cover this interval, with equal width $\sigma_i = 0.25$ mag.

The above expansion can be generalized to account for the color component at each apparent magnitude bin. In particular, we can model the PDF at a given magnitude bin k as a 3D Gaussian of i-band magnitude (X), g-r color (Y) and r-i color (Z). In a compact notation, this function can be written as follows:

$$\mathcal{P}(V|\theta) = \frac{c_k}{(2\pi|U|)^{\frac{3}{2}}} \exp\left[-\frac{1}{2}(V - V_0)^T U^{-1}(V - V_0)\right] \quad (7)$$

where V is a vector of coordinates in the color-color-magnitude space, i.e., $V = \{X, Y, Z\}$, and V_c is the vector of coordinates at $\{X_c, Y_c, Z_c\}$, which corresponds to the center of Gaussian k along the i-band axis and the centroid of the red sequence on the color-color plane, respectively. All the information regarding the shape of the PDF is contained in matrix U , including both the contribution from the intrinsic distribution and the covariance matrix for the photometric errors, C . It can be shown that if the intrinsic model is assumed to be a 3D Gaussian where σ_i is the intrinsic size along the magnitude axis and σ_c is the intrinsic scatter on the color-color plane, matrix U can be expressed as:

$$U = C + \begin{bmatrix} \sigma_i^2 & 0 & 0 \\ 0 & \sigma_c^2(q^2 a^2 + b^2) & \sigma_c^2 ab(1 - q^2) \\ 0 & \sigma_c^2 ab(1 - q^2) & \sigma_c^2(q^2 b^2 + a^2) \end{bmatrix}$$

where θ is the position angle of the Gaussian on the color-color plane w.r.t. the X axis, $a = \sin(\theta)$, $b = \cos(\theta)$ and q is the inverse of the ellipticity. The second term in the above equation accounts for the contribution of the intrinsic distribution on the covariance matrix for the PDF - hereafter C_{int} .

As mentioned before, we need to account for the possible shift of the red sequence centroid with magnitude on the color-color plane. To this end, we model $\{Y_c, Z_c\}$ as:

$$\begin{aligned} Y_c &= Y_0 + Y_1(X - X_{ref}) \\ Z_c &= Z_0 + Z_1(X - X_{ref}) \end{aligned} \quad (8)$$

where X_{ref} is a reference magnitude, for which we choose $X_{ref} = 19$.

Expression 7 is still not a fully-representative model for the observed CMASS PDF, because the CMASS selection has not yet been taken into account. This step is done trivially by applying the CMASS selection matrix, S_{CMASS} . Namely:

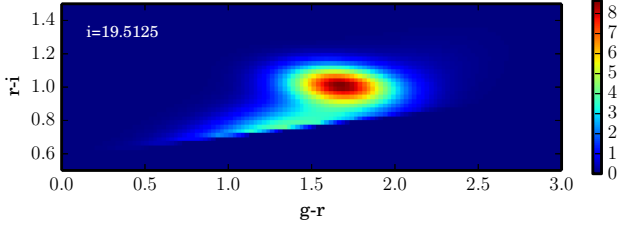


Figure 7. Best-fit model for the CMASS PDF in a redshift slice centered at $z = 0.55$ ($\Delta z = 0.01$) obtained using our analytical deconvolution method. The analytical form of the CMASS PDF contains both the contribution of the intrinsic distribution and the effect of photometric blurring and selection effects.

$$\mathcal{P}_{CMASS}(V|\theta) = \mathcal{P}(V|\theta)S_{CMASS} \quad (9)$$

A single-Gaussian model is certainly a good approximation for the red sequence, but not for the entire CMASS sample, which contains a fraction of blue objects that increases with redshift. In order to take this population into account, we use a double-Gaussian model for the CMASS PDF:

$$\mathcal{P}_{CMASS}(V|\theta) = f_{blue}\mathcal{P}_{CMASS}^{BC}(V|\theta^{(BC)}) + (1 - f_{blue})\mathcal{P}_{CMASS}^{RS}(V|\theta^{(RS)}) \quad (10)$$

where \mathcal{P}_{CMASS}^{BC} is the PDF for the blue cloud, \mathcal{P}_{CMASS}^{RS} is the PDF for the red sequence and f_{blue} is the observed fraction of blue objects in the sample (blue objects meaning non-red sequence objects). With this extension, the total number of fitting parameters is 19 ($2 \times 9 + 1$). In the following sections we discuss possible priors that can reduce the number of parameters in our PDF model.

Table 2 lists all parameters of the PDF for each individual Gaussian function, along with the parameters accounting for the fraction of blue objects, f_{blue} . In addition, we include β , the error scale factor for the covariance matrix C .

5.2 Computation of best-fit parameters

The determination of best-fit parameters is performed by simply minimizing the $-\log\mathcal{L}$. The likelihood \mathcal{L} for a given set of parameters can be obtained at each redshift slice by evaluating our observed CMASS PDF at the position of each object in our 3D space, and summing the probabilities.

The above optimization method provides a best-fit intrinsic distribution at each redshift slice. As part of this process, it provides m_* which, as we demonstrate in subsequent sections, can be trivially transformed into M_* , the characteristic absolute magnitude of the LF.

Our method also incorporates an easy way to compute ϕ_* , the normalization of the RS LF. We have assumed for simplicity that ϕ_* , the normalization of the Schechter function that represent the RS intrinsic distribution, is equal to 1. The predicted fraction of objects that are selected for the

CMASS sample, after convolving with the error model, is given by:

$$n_{pred} = \sum_i \mathcal{P}_{CMASS}^{RS}(V_i|\theta)\Delta X\Delta Y\Delta Z \quad (11)$$

where of course this computation must be performed prior to any normalization. If the total number of real CMASS objects detected within the corresponding redshift slice is given by n_{obs} , the value of ϕ_* for the RS LF can be calculated by:

$$\phi_*^{RS} = \frac{(1 - f_{blue})\frac{n_{obs}}{n_{pred}}}{V_{max}} \quad (12)$$

where $(1 - f_{blue}) \times \frac{n_{obs}}{n_{pred}}$ is the predicted number of intrinsic RS objects and V_{max} is the maximum volume in the corresponding redshift slice. A similar procedure can be used to obtain ϕ_*^{BC} .

5.3 Priors for the intrinsic distribution

Our histogram deconvolution method provides important information regarding the general shape of the intrinsic distributions, that can be used to place constraints on the analytical model for the CMASS PDF described above. Such conclusions are, as discussed before, in good agreement with the general predictions from SPS models.

In particular, the following information, that was gathered from the histogram deconvolution method, the SPS models and the analytical deconvolution itself, is incorporated into our model for the intrinsic distribution:

- The red sequence is consistent with a single point on the color-color plane, with all the observed scatter being due to photometric errors, i.e., $q^{RS} = 0$, $\sigma^{RS} = 0$.
- The location of the red sequence in the color-color plane should, in principle, have a slight dependence on magnitude.
- We have checked that our error model alone cannot account completely for the scatter seen on the blue side, even though a simple 1-dimensional Gaussian, a line in the color-color plane, is certainly not a bad approximation. We avoid therefore imposing $q = 0$ for the blue cloud. Due to the severe incompleteness affecting the blue side, the blue cloud is only modeled for the sake of subtracting its contribution on the red side.
- Due to the severe incompleteness affecting the blue side at most redshifts (the effect of the d_\perp cut), allowing too much freedom to the model when finding the location of the blue cloud centroid might result in unphysical solutions. In fact, the BC centroid tends to be pushed towards the green valley region, basically meshing with the RS centroid.

With the above considerations, the intrinsic component of the covariance matrix in Equation 7, for the single-point red sequence, can be simply expressed as:

$$C_{int}^{RS} = \begin{bmatrix} \sigma_i^2 & 0 & 0 \\ 0 & 0 & 0 \\ 0 & 0 & 0 \end{bmatrix}$$

which is equivalent to a Delta function on the color-color plane, with position given by Y_0^{RS} , Y_1^{RS} , Z_0^{RS} , Z_1^{RS} .

As for the blue cloud component, we keep C_{int} in its general form, namely:

$$C_{int}^{BC} = \begin{bmatrix} \sigma_i^2 & 0 & 0 \\ 0 & \sigma_c^2(q^2a^2 + b^2) & \sigma_c^2ab(1 - q^2) \\ 0 & \sigma_c^2ab(1 - q^2) & \sigma_c^2(q^2b^2 + a^2) \end{bmatrix}$$

but we impose $Y_1^{BC} = 0$ and $Z_1^{BS} = 0$. We also include the condition $Y_0^{BC} + Z_0^{BC} = 1.7$, independently of redshift. By doing so, we can fix the centroid of the blue cloud at $g - i = 1.7$, ensuring an adequate BC/RS separation. This value was chosen by examining the distribution of FSPS models (Figure 6) and the distribution of objects in the PRISM Multi-object Survey (PRIMUS, Coil et al. 2011; Cool et al. 2013), which is not affected by a color cut. We have also checked, and this is visible in Figure 6, that the observed centroid of the blue cloud is stable as we move across redshift, due to the typical shape of the SED for blue galaxies, which lack a 4000 Å Balmer break.

5.4 Error scale factor

Our error model, built from the Stripe 82 multi-epoch data, should account for variations in photometric quality as a function of colors and magnitudes in BOSS. However, as we mention in Section 3, we could expect some global differences between BOSS and Stripe 82 that might make the convergence of our algorithm difficult or even lead to erroneous solutions for the intrinsic distributions.

The convergence of our histogram deconvolution algorithm depends strongly on the value of β , the error scale factor. In fact, convergence is only achieved for $\beta < 1$; $\beta \simeq 0.93$ is the value that provides the best solutions. This implies that the photometric quality of BOSS is slightly underestimated by assuming a model based on Stripe 82.

The above result is confirmed when we use our favored analytical deconvolution method. While the algorithm converges for any reasonable value of β , a value of $\beta = 1$ produces too much scatter for the RS, as compared to the data, even if the RS is modeled as a single point in the color-color plane. Again, a value of $\beta \sim 0.92$ improves the likelihood considerably. A visual inspection of the residuals, shows, however, that a constant value for β has opposite effects towards each side of the CMASS magnitude range. In particular, it tends to make the distributions too broad at the bright end and too narrow at the faint end. In order to avoid these effects, we adopt the following empirically-developed functional form for $\beta(i)$:

$$\beta(i) = \left[\frac{1 + 10^{0.6(X - i_0 + \Delta i)}}{1 + 10^{0.6(X - i_0)}} \right]^{1/2} \quad (13)$$

where X is the i -band apparent magnitude and $i_0 = 19.5$. The optimal value for Δi is obtained by fitting for this parameter in multiple redshift slices within the redshift range $0.52 < z < 0.65$, and taking the average value of all measurements.

6 RESULTS

6.1 Algorithm performance and the best-fit intrinsic distributions

Figure 7 displays our best-fit model for the CMASS PDF in the redshift slice centered at $z = 0.55$, for an apparent magnitude $i = 19.5$. As described before, this PDF provides the probability density of finding a galaxy at any given point in the color-color plane, assuming our best-fit error-deconvolved intrinsic distribution, our Stripe 82 error model and the CMASS selection function. Figure 7 shows that the CMASS PDF is consistent, generally speaking, with the observed CMASS distribution. In order to demonstrate this, we have generated a mock distribution assuming this best-fit CMASS PDF, with the same number of objects as those passing the CMASS selection in the $z = 0.55$ redshift slice. Figure 8 compares these two distributions, which are presented in bins of magnitude ($\Delta i = 0.1$) and colors ($\Delta g - r = 0.1$, $\Delta r - i = 0.1$). In particular, we show the data, the model, the data-model residuals and the red sequence and blue cloud components, respectively.

A visual inspection of the residuals in Figure 8 reveals that our CMASS PDF can reproduce, to a high level of accuracy, the shape and main characteristics of the observed CMASS distributions and also account for its magnitude dependence. As expected, most discrepancies appear towards the bright end (i.e. $i \lesssim 19$) where statistics are remarkably poorer and we are dominated by cosmic variance.

A good way to assess the significance of the residuals shown in Figure 8, as far as the computation of the LF is concerned, is to compare the observed number counts with those predicted by our model. This comparison is provided in Figure 9 for 20 redshift slices from $z = 0.51$ to $z = 0.70$. As expressed before, below $z \sim 0.52$ the data are too incomplete to be used for constraining the intrinsic distributions. In each panel, we represent the number of objects as a function of magnitude - $N(m)$ - for the data (crosses), the combined model in observed space (green solid line), the RS and the BC components separately (red dashed line and blue dashed line, respectively) and the intrinsic RS distribution (magenta line). As Figure 9 illustrates, the agreement between the model and the data is quite good across the redshift range considered, with discrepancies always below 3-4%. Figure 9 also illustrates the composition of our model in observed space, with a prominent RS component peaking at progressively fainter magnitudes as we move to higher redshifts. The BC component, which appears to be brighter, is enhanced at higher redshift, as a result of the fact that the d_{\perp} cut and the sliding cut are progressively less stringent. As expected, the intrinsic RS number counts keep rising exponentially when the effect of these color cuts is removed. In order to illustrate the significance of the discrepancies observed in Figure 9 as far as the computation of the LF is concerned, Figure 10 displays number counts at $z = 0.55$ in a more common fashion, i.e. $\log_{10}[N(m)/\Delta m/A_{eff}]$, where $\Delta m = 0.1$ and A_{eff} is the effective area of the DR10 LSS footprint. As expected, the small discrepancies visible in Figure 10 are not noticeable when the number counts are presented in this manner. This clearly indicates that these dis-

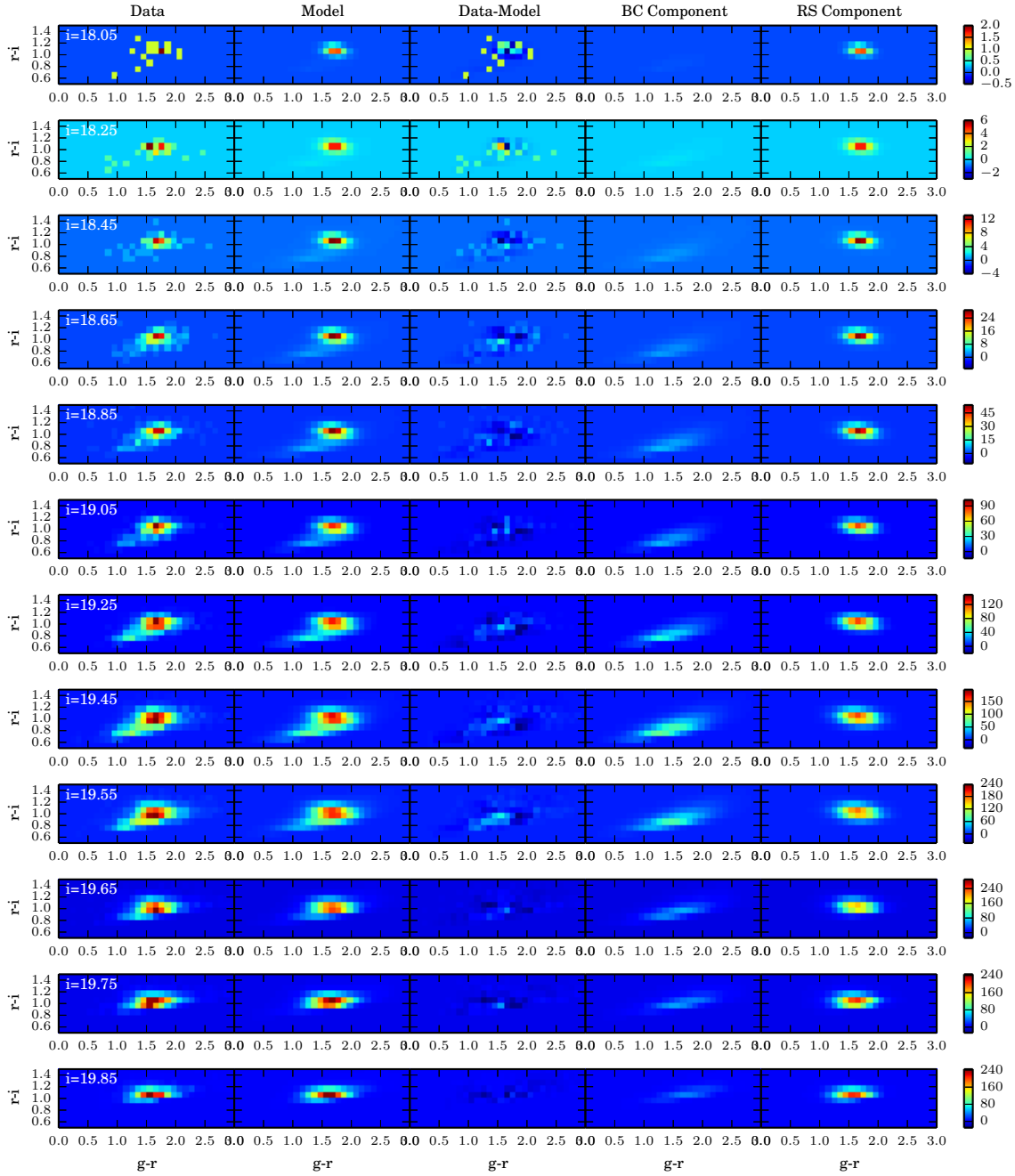


Figure 8. Best-fit model in observed space obtained using the analytical deconvolution method as compared with the data, in a redshift slice of width $\Delta z = 0.01$ centered at $z = 0.55$. From left to right: data, model in observed space, data-model residuals, model for the red sequence (RS) component in observed space and model for the blue cloud (BC) component in observed space, respectively, in $g-r$ vs $r-i$ color-color diagrams for 12 different magnitude bins. The bin size is 0.1 in all three quantities. The same color code applies to all distributions in the same panel, but color codes vary for different panels. The typical photometric error quoted in the catalog is ~ 0.20 for the $g-r$ color and ~ 0.08 for the $r-i$ color. Our CMASS PDF can reproduce, to a high level of accuracy, the shape and main characteristics of the observed CMASS distributions and also account for its magnitude dependence.

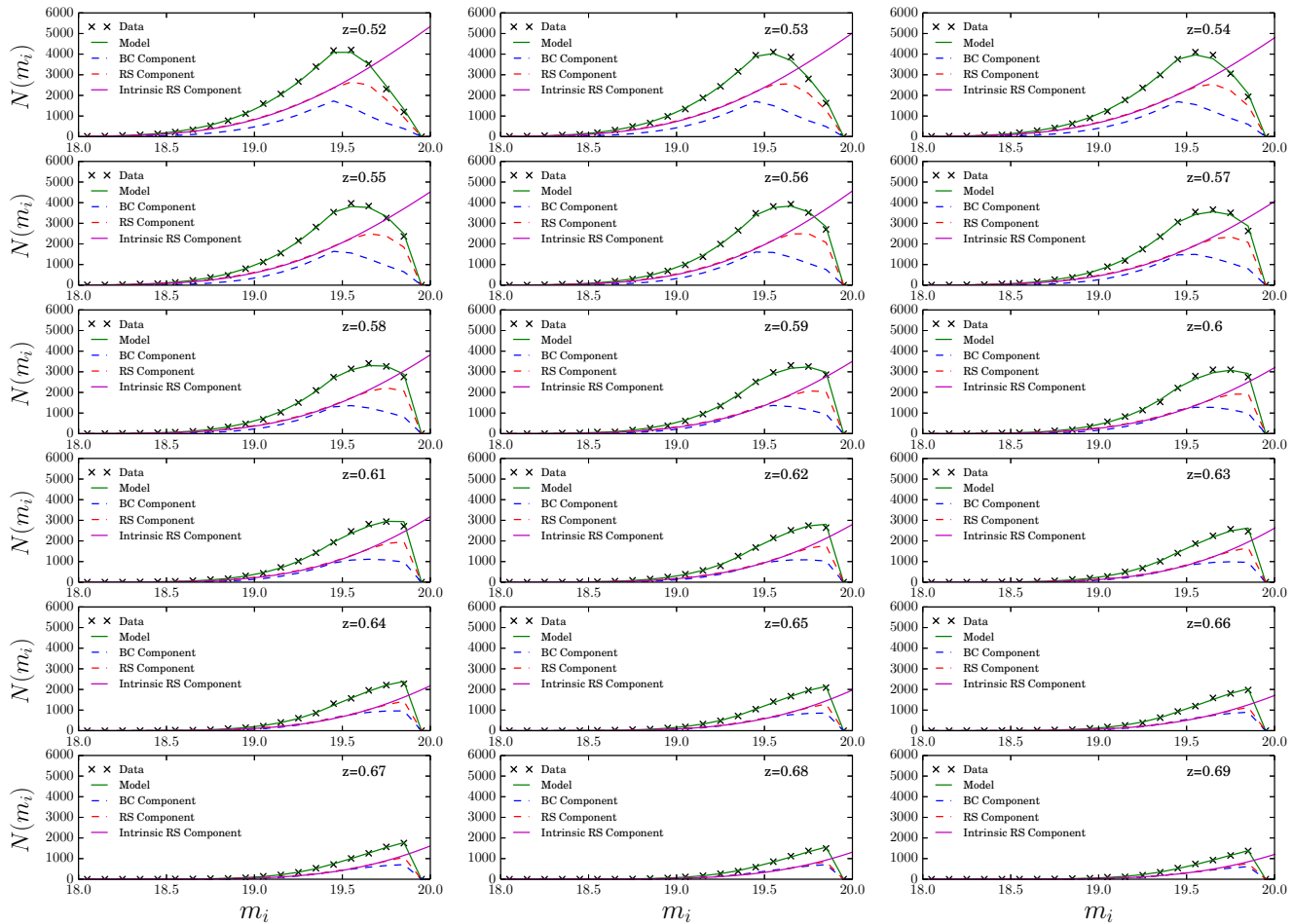


Figure 9. The i-band number counts for both the data and the model at 18 redshift slices from $z = 0.51$ to $z = 0.70$. Each panel shows the number of galaxies in each magnitude bin, $N(m)$, as a function of magnitude for the data (black crosses), the model in observed space (green solid line), the RS component (red dashed line), the BC component (blue dashed line) and the intrinsic RS model (magenta solid line). This figure illustrates that the agreement between the model and the data is quite good across the redshift range considered, with discrepancies always below 3-4%

crepancies will be negligible when compared to the typical measurement errors associated with the computation of the LF. Only at the bright-end, where the data are dominated by cosmic variance, are there some non-negligible discrepancies. Note that $i < 18.5$ roughly corresponds to $^{0.55}M_i \lesssim -24$ at $z = 0.55$, i.e., the very luminous end of the LF.

Finally, in Figure 11, we show the best-fit intrinsic distributions at $z = 0.55$ in progressively fainter i-band magnitude bins in logarithmic scale. The shape of the RS and the BC in a color-color diagram is presented in the left-hand column. The RS is, by definition, a point that shifts slightly towards redder colors for fainter magnitudes. The BC, on the other hand, is consistent with a diffuse distribution that extends through the red side of the diagram, where the RS is embedded. In the right hand column, we show the distribution of g-i colors, a quantity that is often used to separate the RS and the BC. Note that the bluer side of these di-

agrams exceeds the CMASS selection range, where we can confidently report the shape of the BC intrinsic distribution.

Interestingly, and independently of the priors that we choose, our model requires an intrinsic BC component that extends through the red side of the color-color diagram in order to achieve an acceptable agreement with the number counts. This result implies that there are BC galaxies that are intrinsically redder than the RS itself. Although this conclusion might appear contradictory, the existence of spirals with unusually red colors has been thoroughly documented in the literature (e.g., Masters et al. 2010a,b, Wolf et al. 2009, Bundy et al. 2010). In this sense, some consensus has been reached that, although in the majority of cases these red colors are likely to be due to dust, there exists a significant fraction of purely passive red spirals, without a large amount of dust reddening. In following sections, the expected fraction of BC objects within the entire sample

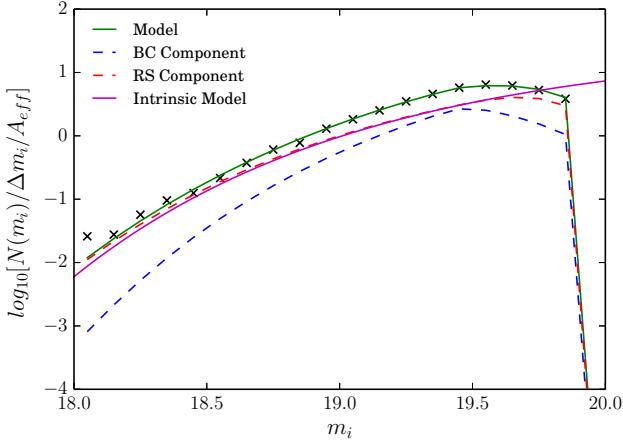


Figure 10. The *i*-band number counts for both the data and the model at $z = 0.55$ expressed as the logarithm of the number of galaxies per unit magnitude bin and effective area in the DR10 LSS footprint. The lines represent: the data (black crosses), the model in observed space (green solid line), the RS component (red dashed line), the BC component (blue dashed line) and the intrinsic RS model (magenta solid line). This figure illustrates the excellent agreement between the model and the data, with only small discrepancies that have little effect on the computation of the RS LF.

along with the fraction of BC objects on the red side of the color-color plane will be provided.

6.2 Redshift evolution of best-fit parameters

The performance of the analytical deconvolution method is excellent for redshift slices within the redshift interval $0.53 \lesssim z \lesssim 0.70$. Below $z \simeq 0.53$, results become progressively noisier as the CMASS RS is more and more incomplete. Above $z \simeq 0.65$, our method converges and provides acceptable residuals, but the effective apparent magnitude range is so small that the LF is rather unconstrained.

Figure 12 shows the redshift evolution of the main RS best-fit parameters for our fiducial model, described in previous sections (red), for a simpler model where the centroid of the RS is assumed to be fixed on the color-color plane ($Y_1 = 0$, $Z_1 = 0$), and for a model where $Y_1 = Z_1 = -0.05$. We show here the fraction of blue objects in the sample, f_{blue} , the characteristic apparent magnitude m_* and the (*g*-*i*) color of the RS centroid at the reference magnitude $i = 19$ ($Y_0 + Z_0$).

The fraction of blue objects in the CMASS sample (left-hand panel) increases from a value of ~ 0.38 at $z = 0.50$ to ~ 0.50 at $z = 0.70$. This increase implies that a progressively larger fraction of the BC is passing the d_\perp cuts. These values for f_{blue} might seem rather high, however, as previously mentioned, f_{blue} corresponds to the fraction of all BC objects in the sample, including the part of the BC distribution that extends through the red side of the color-color plane.

The middle panel of Figure 12 shows how m_* fades from a value of ~ 20.2 to ~ 21 within the redshift range consid-

ered. This trend is misleading, due to the effect of redshift. In following sections we will discuss the evolution of the LF, where this effect is subtracted and only the intrinsic evolution of the galaxy population remains. More interesting than the trend itself is the fact that m_* is fainter than the CMASS faint limit ($i = 19.9$) across the entire redshift range, illustrating the extreme luminosity of the sample.

The right-hand panel of Figure 12 shows the redshift evolution of the intrinsic RS *g*-*i* color. As we discuss in following sections, a great advantage of our modeling is that it allows an accurate estimation of the location of the RS color centroid. This can be used to place tight constraints on the stellar population properties of the RS population. However, Figure 12 shows an anomalous behavior near $z = 0.60$. As can be seen in the right-hand plot, there is a strong discontinuity around this redshift that is mitigated, but not eliminated, when we allow for a color-magnitude relation for the RS. Note that due to the effect of redshift, the observed color distribution moves to redder colors at higher redshift. Below $z \lesssim 0.60$, the BC is essentially undetected in the CMASS sample due to the d_\perp cut. It is only above $z \simeq 0.60$ that the BC starts to appear in a way that we can actually place constraints on its shape. Redshift $z \simeq 0.60$ is therefore a transition redshift where divergent solutions appear for some of the best-fit BC parameters. This divergence also affects the RS best-fit parameters. Dealing with this effect in a proper manner will require further investigation, given that it is basically caused by a strong limitation of the data itself.

6.3 Completeness in the CMASS sample

The model for the covariance matrix described in Section 3, along with the best-fit model for the intrinsic distribution, allow us to place the CMASS data into the context of the underlying distribution from which it was collected, and to understand the effect of selection and photometric errors. This analysis is done by estimating the completeness of the CMASS sample as a function of magnitude, color and redshift. Completeness is defined here as *the fraction of objects from the intrinsic distribution (in intrinsic space) within a given range of magnitude, color and redshift that is expected to pass the CMASS selection, assuming our photometric error model*.

By taking random deviates of a Gaussian probability distribution characterized, at each bin, by the elements of our covariance matrix model evaluated at the corresponding bin, and recording the number of trials passing the CMASS selection, we can estimate the probability for a galaxy randomly located within our 3D space to be selected. By combining this selection probability with our best-fit intrinsic distribution, we can obtain an estimate for completeness in the CMASS sample. We can only confidently report completeness for the RS, due to the nature of the CMASS selection. In the left-hand panel of Figure 13 we show completeness as a function of magnitude for the RS distribution in nine redshift slices from $z = 0.50$ to $z = 0.70$. As expected, the sample is complete for the RS at the bright end ($i \lesssim 19.4$) across the entire redshift range. Between $i \simeq 19.4$

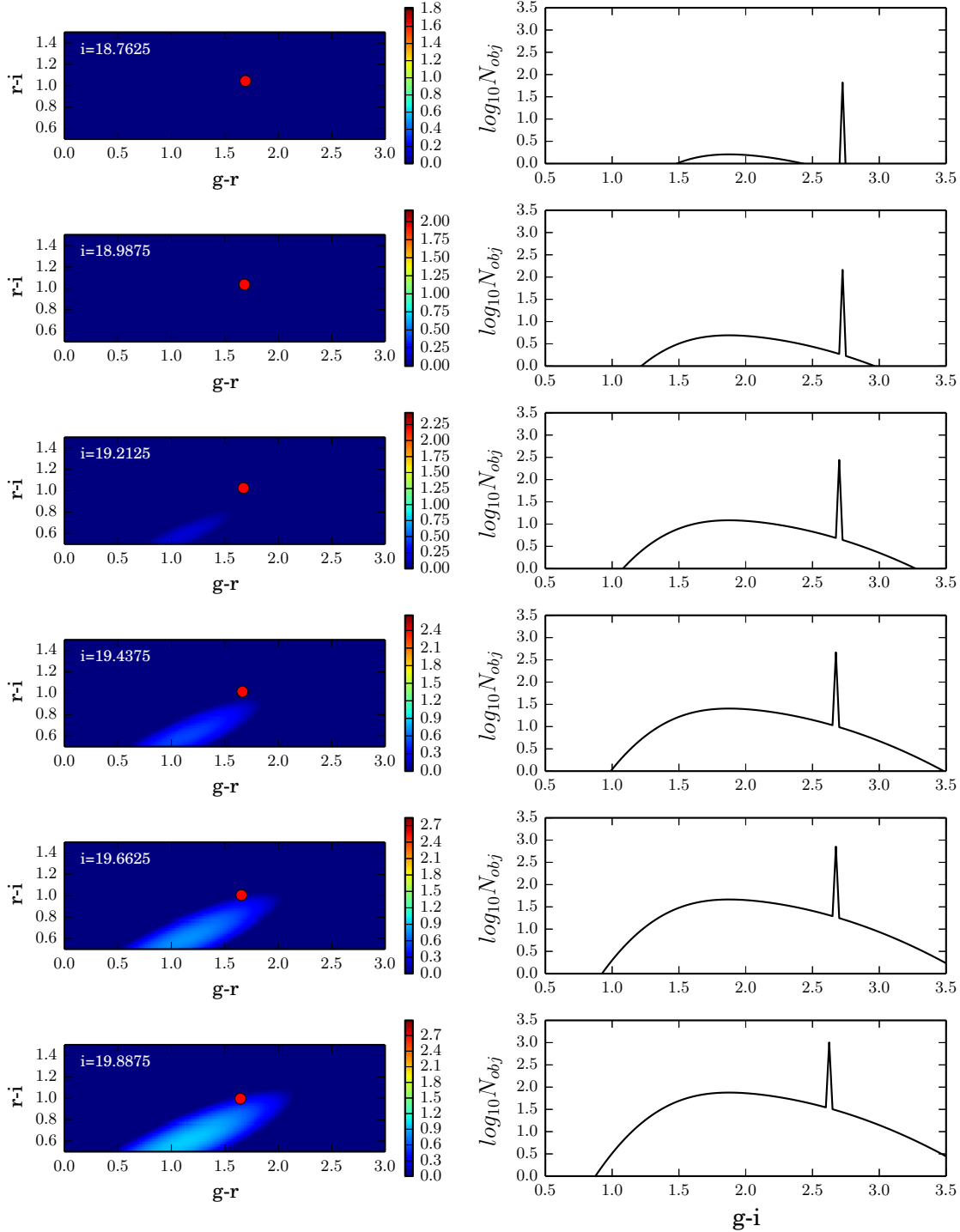


Figure 11. Best-fit intrinsic distributions at $z = 0.55$ for six i -band apparent magnitude bins (in logarithmic scale). Left: RS (red) and BC (blue) intrinsic distributions in the color-color diagram, respectively. The point representing the RS has been exaggerated for the sake of clarity. Right: The corresponding best-fit intrinsic distribution of $g-i$ colors, also in logarithmic scale. Note that the bluer side of this diagrams (right-hand panels) exceeds the CMASS selection range, where we can confidently report the shape of the BC intrinsic distribution. The RS is, by definition, a point that shifts slightly towards redder colors for fainter magnitudes. The BC, on the other hand, is consistent with a diffuse distribution that extends through the red side of the diagram, where the RS is embedded.

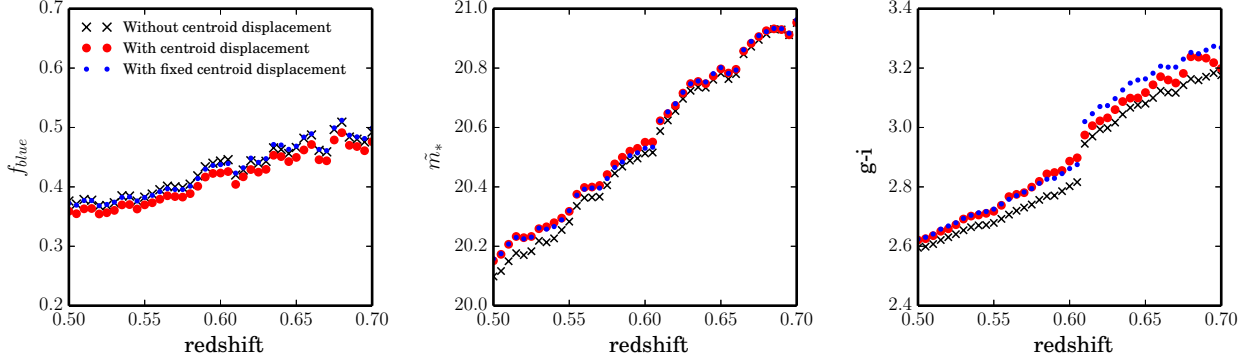


Figure 12. Redshift evolution of best-fit parameters f_{blue} (observed fraction of BC objects in the sample) and m_* (RS characteristic apparent magnitude), along with the (g-i) RS centroid at the reference magnitude $i = 19$. Three different models are shown here: our fiducial model with centroid displacement (big red circles), the same model with fixed centroid (black crosses) and a model where Y_1 and Z_1 , the slopes of the color-magnitude relations, have been set to -0.05 (small blue dots).

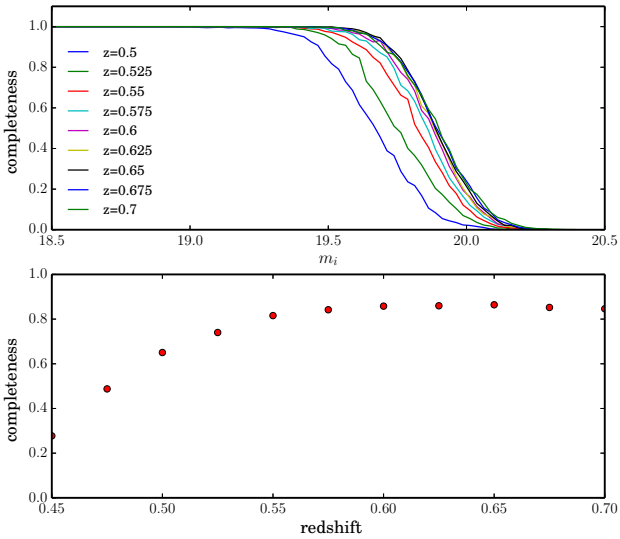


Figure 13. Completeness in the CMASS sample. Upper panel: RS completeness as a function of i-band magnitude in the CMASS sample for nine redshift slices within the redshift range $0.5 < z < 0.7$. Lower panel: Integrated RS completeness as a function of redshift. As expected, the sample is complete for the RS at the bright end ($i \lesssim 19.4$) across the entire redshift range. Between $i \simeq 19.4$ and $i \simeq 19.7$, completeness declines quite abruptly, this effect occurring at progressively fainter magnitudes for higher redshifts. The overall RS completeness increases from a very low value at low redshift to ~ 0.8 at $z = 0.55$, reaching a plateau around ~ 0.82 at $z \gtrsim 0.52$

and $i \simeq 19.7$, completeness declines quite abruptly, this effect occurring at progressively fainter magnitudes for higher redshifts. The shape of the completeness function is determined by the d_{\perp} cut and the sliding color-magnitude cut being applied to a RS distribution that is progressively redder at higher redshifts. The right-hand panel of Figure 13 provides the integrated RS completeness as a function of

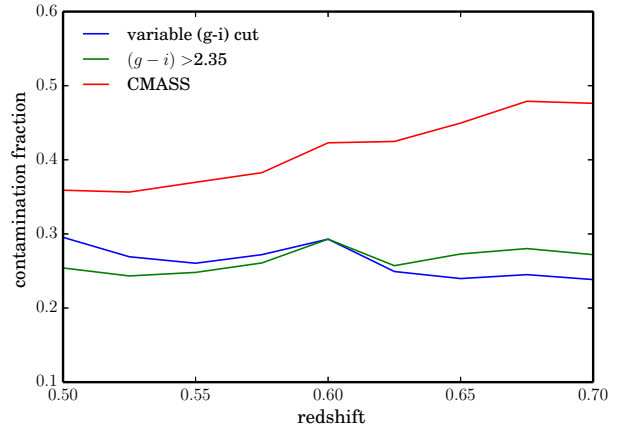


Figure 14. The intrinsic fraction of BC objects contaminating the red side of the color-color diagram of the total number of red objects. The red side is defined here in two different ways: using a fixed redshift-independent g-i demarcation at $g - i = 2.2$, $g - i = 2.3$ and $g - i = 2.4$, respectively, and using a redshift-dependent demarcation that is obtained empirically from the observed color-color distributions. Also shown in the plot is the total fraction of BC objects in the CMASS.

redshift. The RS completeness increases from a small value at low redshift to ~ 0.8 at $z = 0.55$, reaching a plateau of ~ 0.82 at $z \gtrsim 0.52$.

As previously pointed out, it would be risky to report completeness/LF for the BC, given the insufficient constraints in the CMASS data. However, we can certainly provide an accurate estimation of the fraction of BC objects in the sample, i.e., the f_{blue} parameter, and the contamination from intrinsically BC objects on the red side of the color-color diagram. We emphasize here the difference between *the red side*, which is commonly defined by a simple color demarcation (e.g., $g - i = 2.35$) in observed space, and the RS, which is a distinct galaxy population, modeled here as a delta function in the color-color plane, and

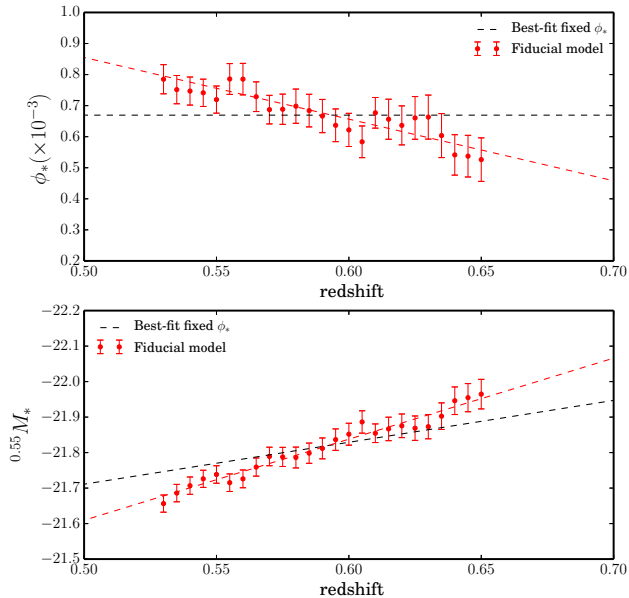


Figure 15. Redshift evolution of the computed Schechter parameters ϕ_* and $^{0.55}M_*$ for the bright end of the red sequence luminosity function. Both the results for our fiducial model (red) and for the best-fit constant- ϕ_* model (black) are provided within the redshift range $0.53 < z < 0.65$. The red dashed line represents a linear fit to the fiducial model results obtained within our high confidence redshift interval (shaded regions). The errors shown are the statistical errors of the fit. The error bars correspond to 2σ on each side of the measurement.

intrinsically separated from the BC component. Figure 14 shows this contamination as a function of redshift assuming two g-i color demarcations. Firstly, we use a fixed g-i cut at $g - i = 2.35$. Under such condition, the contamination hovers around $\sim 25\%$ within the redshift range considered. In order to account for the effect of redshift on the color distributions, we also assume a redshift-dependent demarcation that is obtained empirically from the observed color-color distributions themselves. This approach decreases the contamination from ~ 0.30 at $z = 0.50$ to ~ 0.25 at $z = 0.70$. Interestingly, even though the completeness of the BC increases remarkably towards higher redshifts (i.e., we have more BC objects at high redshift), the fraction of BC objects that contaminate the red side remains essentially constant. Figure 14 also displays the fraction of BC objects in the sample (the f_{blue} parameter). This fraction does experience a considerable increase as a function of redshift, from $\sim 36\%$ at $z = 0.50$ to $\sim 46\%$ at $z = 0.70$. The total fraction of intrinsic BC objects (not just objects with blue colors) in the CMASS sample is 37%.

6.4 The high-mass end of the red sequence luminosity function of galaxies

Our analytical deconvolution method provides, by construction, a straightforward approach to determine the luminosity function for both the RS and the BC, although only the first

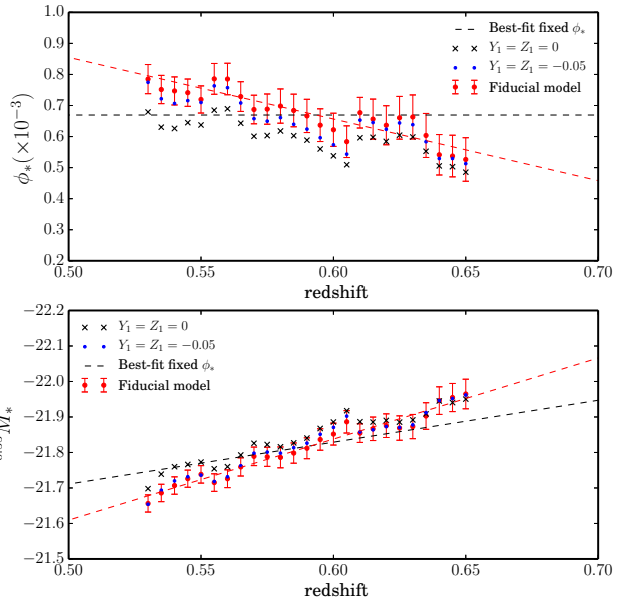


Figure 16. The same as in Figure 15 but including two alternative, less probable models. Black crosses show a best-fit model with fixed centroid ($Y_1 = Z_1 = 0.0$) and blue dots represent a model where $Y_1 = Z_1 = -0.05$.

one is reported here. These LFs are modeled as Schechter functions where we have assumed $\alpha = -1$ for the sake of simplicity. This choice is also motivated by the insufficient constraints on the faint-end slope that we can extract from the CMASS sample. The ϕ_* Schechter parameter is estimated for the RS component and for each redshift slice in the way described in Section 5.2. Here, the maximum volume is assumed to be constant within the corresponding redshift slice. Neglecting any $1/V_{max}$ effects is certainly a reasonable approximation considering the width of our redshift slices and the apparent magnitude range of the CMASS selection. The typical distance modulus variation within our redshift slices is ~ 0.05 mag, which is of the order (if not smaller) of the typical i-band magnitude error.

The absolute magnitude M_* parameter is directly derived by transforming the best-fit (apparent magnitude) m_* parameter. The rest-frame absolute magnitude of an object at an emitted passband Q , M_Q , can be derived from the apparent magnitude measured at an observed-frame passband R , m_R , as follows:

$$M_Q = m_R - DM(z) - K_{QR}(z) \quad (14)$$

where DM is the distance modulus (that depends on the cosmological parameters), z is the redshift and K_{QR} is the K-correction between passbands R and Q (in most cases, including this work, both the emitted and the observed-frame passbands coincide). For the K-correction we opt to blueshift the rest-frame redshift to $z = 0.55$. The motivation for this choice is two-fold. First, the $^{0.55}i$ passband is covered within the entire CMASS redshift range. Second, K-

correcting to a redshift that is close to the mean redshift of the sample reduces the correction itself and, therefore, the uncertainties associated with it. Finally, Equation 14 often includes an extra term called the evolution correction, that accounts for the intrinsic luminosity evolution of each galaxy from z to the chosen rest-frame redshift. Again, the size of the CMASS sample allows us to split the sample in very narrow redshift bins, where evolutionary effects are negligible. We will, however, address the global evolution of the luminosity function by comparing our results with predictions from stellar population models.

Average K-corrections to $z_0 = 0.55$ are derived, for each bin in the color-color plane, using the extensive grid of physically plausible FSPS models described in Section 4.1. The fact that the RS intrinsic distribution is modeled as a delta function on the color-color plane helps simplify the computation here. Moreover, the computed displacement of the RS centroid within the CMASS magnitude range is rather small (i.e., < 0.1), so we can simply take the average of the K-correction within this magnitude range. We have checked that accounting for the color-magnitude relation for the RS when estimating K-corrections does not change our results for the LF in any significant way.

Figure 15 shows the redshift evolution of best-fit Schechter parameters Φ_* and $^{0.55}M_*$, within our high-confidence redshift interval (shaded region), for our fiducial model. Results outside this region are less reliable, due to the high incompleteness of the sample, so we rely on the extrapolation of the following linear fit:

$$\begin{aligned} \Phi_* &= (-1.9854 z + 1.8477) \times 10^{-3} \text{ Mpc}^{-3} \text{ mag}^{-1} \\ ^{0.55}M_* &= -2.2834 z - 20.4677 \end{aligned} \quad (15)$$

The errors shown in Figure 15 are the statistical errors of the fitting procedure, obtained by analyzing the behavior of χ^2 around the best-fit values of the fitting parameters (we choose to show $2\text{-}\sigma$ error bars on each side of the points for the sake of visibility). We have checked, however, that a bootstrap resampling analysis yields error bars of similar size.

We also present in Figure 15 the best-fit Φ_* assuming passive evolution (black dashed line, upper panel). The passive evolution assumption implies for a galaxy population that Φ_* remains constant with redshift. Our best-fit value, which is computed by modeling the χ^2 as a function of Φ_* and M_* , is equal to $(6.693 \pm 0.042) \times 10^{-4} \text{ Mpc}^{-3} \text{ mag}^{-1}$. Fixing Φ_* to a constant value flattens the M_* - z relation considerably. The $^{0.55}M_*$ - z relation corresponding to this best-fit fixed- Φ_* is represented by a black dashed line in the bottom panel of Figure 15. This trend implies a fading rate of $\Delta^{0.55}M_*/\Delta z = 1.180 \pm 0.001 \text{ mag per unit redshift}$ for the passive evolution hypothesis.

As previously seen, the computation of the RS LF from the CMASS sample is a complex task, due to strong selection effects and large photometric errors. In this sense, some of our model choices have an impact on the computed LFs. In particular, neglecting the displacement of the RS centroid with magnitude tends to flatten the Φ_* - z relation. In order to illustrate this effect, we show in Figure 16 the LF

Redshift	$\phi_* \times 10^{-3} \text{ Mpc}^{-3} \text{ mag}^{-1}$	$^{0.55}M_*$
0.530	0.7850 ± 0.0234	-21.6562 ± 0.0120
0.535	0.7514 ± 0.0227	-21.6859 ± 0.0122
0.540	0.7469 ± 0.0225	-21.7068 ± 0.0122
0.545	0.7412 ± 0.0219	-21.7260 ± 0.0120
0.550	0.7190 ± 0.0210	-21.7383 ± 0.0122
0.555	0.7857 ± 0.0247	-21.7151 ± 0.0123
0.560	0.7853 ± 0.0250	-21.7259 ± 0.0125
0.565	0.7287 ± 0.0239	-21.7592 ± 0.0127
0.570	0.6871 ± 0.0230	-21.7890 ± 0.0130
0.575	0.6883 ± 0.0243	-21.7800 ± 0.0134
0.580	0.6980 ± 0.0275	-21.7861 ± 0.0146
0.585	0.6840 ± 0.0262	-21.7982 ± 0.0142
0.590	0.6664 ± 0.0260	-21.8118 ± 0.0147
0.595	0.6366 ± 0.0263	-21.8365 ± 0.0151
0.600	0.6218 ± 0.0266	-21.8517 ± 0.0154
0.605	0.5834 ± 0.0255	-21.8863 ± 0.0157
0.610	0.6768 ± 0.0246	-21.8545 ± 0.0131
0.615	0.6562 ± 0.0322	-21.8666 ± 0.0165
0.620	0.6364 ± 0.0314	-21.8754 ± 0.016
0.625	0.6600 ± 0.0340	-21.8688 ± 0.0171
0.630	0.6631 ± 0.0354	-21.8729 ± 0.0170
0.635	0.6035 ± 0.0354	-21.9026 ± 0.0187
0.640	0.5413 ± 0.0325	-21.9460 ± 0.0194
0.645	0.5370 ± 0.0335	-21.9547 ± 0.0198
0.650	0.5261 ± 0.0350	-21.9647 ± 0.0200

Table 3. Best-fit Schechter parameters for the i-band RS LF at multiple redshift slices from $z = 0.53$ to $z = 0.65$. The LF has been k-corrected to $z = 0.55$. We have assumed $\alpha = -1$.

for three different models: our fiducial model (red), a model where $Y_1 = Z_1 = -0.05$ (blue) and a model where centroid displacement is neglected (black). The following linear relations are obtained for the fixed centroid model:

$$\begin{aligned} \Phi_* &= (-1.41558 z + 1.43519) \times 10^{-3} \text{ Mpc}^{-3} \text{ mag}^{-1} \\ ^{0.55}M_* &= -1.83534 z - 20.75916 \end{aligned} \quad (16)$$

The Schechter parametrization presented in Figures 15 and 16 represents exclusively the bright end of the RS LF, i.e. the magnitude range where we have data. Any extrapolation towards the faint end would lead to erroneous outputs. In fact, when Φ_* is not fixed, the Schechter parameters are

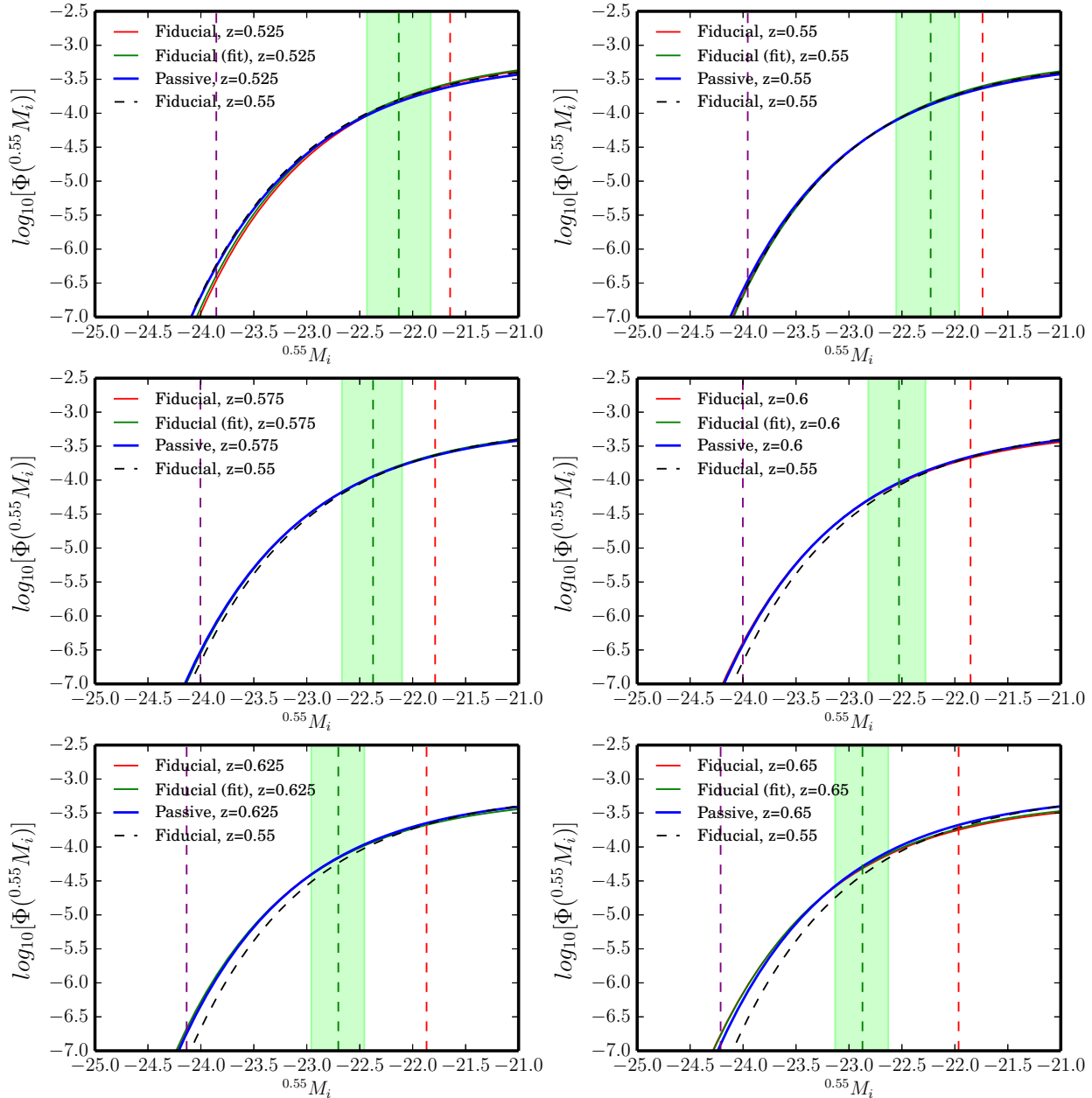


Figure 17. The bright end of the $^{0.55i}$ -band RS LF in six redshift slices between $z = 0.525$ and $z = 0.65$. Each panel shows the RS LF computed with our fiducial model at the corresponding redshift (solid red line), the RS LF obtained with the linear fits to the Schechter parameters of the fiducial model at the corresponding redshift (solid green line) and our best-fit passive evolving model for the RS LF (solid blue line). In addition, we show for reference the fiducial model for the RS LF at $z = 0.55$ (dashed black line). Vertical dashed lines represent, from left to right: a bright-end reference magnitude corresponding to the value below which the total number of objects in the CMASS sample at that particular redshift is 25 (purple line); the 0.5-completeness limit of the sample (green line, including as well in a shaded region the 0.02 and 0.98 completeness limits) and $^{0.55}M_*$ (red).

highly degenerate at the bright end, so drawing any conclusions from the evolution of these parameters alone can be misleading. As an example, the dimming rate $\Delta^{0.55}M_*/\Delta z$ measured within the range $0.535 \leq z \leq 0.65$ examining only the $^{0.55}M_*$ - z relation is 2.28 mag per unit redshift.

The increase in Φ_* within the entire CMASS redshift range ($0.45 \leq z \leq 0.70$) is of a factor of ~ 2 , assuming the linear fit of Equation 16. This evolution in the Schechter parameters would appear to challenge the somewhat accepted hypothesis of passive evolution for the LRGs. A purely passively-

evolving population of galaxies experiences no merger processes that could trigger star formation or modify the number density.

In order to avoid a misinterpretation of the Schechter parametrization, Figure 17 presents the RS LF in 6 redshift bins within our high-confidence redshift interval ($0.525 < z < 0.65$). In each panel, we show the RS LF computed with our fiducial model at the corresponding redshift (red solid), the RS LF obtained with the linear fits to the Schechter parameters of the fiducial model at the corresponding redshift (green solid line) and our best-fit passive-evolving model for the RS LF (blue solid line). In addition, the fiducial model for the RS LF at $z = 0.55$ is also shown (black dashed line). Vertical dashed lines indicate, from left to right: a bright-end reference magnitude corresponding to the value below which the total number of objects in the CMASS sample at that particular redshift is 25 (purple); the 0.5-completeness limit of the sample (green, including as well in a shaded region the 0.02 and 0.98 completeness limits) and $^{0.55}M_*$ (red). Figure 17 again illustrates the extreme luminosity of the sample, with 50% completeness limits between -22.1 and -22.7 , i.e., $0.6 - 1$ mag brighter than $^{0.55}M_*$ within our high-confidence redshift interval. Importantly, Figure 17 demonstrates that the evolution of the massive-end RS LF is consistent with our best-fit passive-evolution model, with $\Phi_* = (6.6930.042) \times 10^{-4} \text{ Mpc}^{-3} \text{ mag}^{-1}$ and a fading rate of $\Delta^{0.55}M_*/z \simeq 1.180 \pm 0.001$ per unit redshift. However, some deviations from a single passively-evolving Schechter function exist. In order to characterize these deviations properly we define two absolute magnitudes M_{min} and M_{max} so that $\log_{10} \Phi(M_{min}) = -6$ and $\log_{10} \Phi(M_{max}) = -4.5$, respectively. We also define the magnitude difference parameter $\Delta M = |M_{max} - M_{min}|$. This is an alternative way of parametrizing the massive-end of the LF, which is better suited for cases where the magnitude coverage is small. The values of $\log_{10} \Phi(M_{min}) = -6$ and $\log_{10} \Phi(M_{max}) = -4.5$ are defined so that the corresponding M_{min} and M_{max} are brighter than the 50% completeness limit at any redshift. The difference in ΔM between the two extremes of the high-confidence redshift range is ~ 0.07 mag. This difference is small, but indicates some level of differential evolution. Galaxies at a number density of $\log_{10} \Phi(M_{min}) = -6$ have faded by ~ 0.22 mag within the redshift range considered, whereas galaxies at the slightly-fainter end have faded ~ 0.07 mag less within the same redshift range.

Finally, we have checked that the differences between our fiducial model and a model where the color-magnitude relation has been neglected (Figure 16) translate into small differences in the LF itself, due to the anti-correlation of the Schechter parameters.

6.5 The fading rate of the high-mass end of the red sequence

The unprecedented size of the CMASS sample allows measurement of the fading rate of the RS LF within the redshift range $0.525 \leq z \leq 0.650$ with extraordinary accuracy. Even though we use a narrow redshift range, the precision of our measurement can be used to place tight constraints on the

age of the LRG population at $z \simeq 0.55$. As we discussed in the previous section, the computed fading rate for our best-fit passive-evolving model is $\Delta^{0.55}M_*/\Delta z \simeq 1.18$ mag per unit redshift. For the fiducial model, which is the model that achieves a better agreement with the observed number counts, a constant- Φ_* Schechter function (passive evolution) is not favored anymore, although deviations are very small. At M_{min} we find that galaxies have faded by 0.07 mag more than their less luminous counterparts. This would imply a fading rate of $\Delta^{0.55}M_*/z \simeq 1.76$ mag per unit redshift, although for non-passive evolution the concept of fading rate becomes less meaningful. In any case, this differential fading for the massive end of the RS LF, where brighter galaxies fade more rapidly than the fainter ones, appears to suggest some differences in the SFH of these galaxies. However, this detection is fairly small as compared to the uncertainties associated with the computation of the RS LF. Moreover, differences only become non-negligible at an extremely bright magnitude range (M_{min}), where we are unavoidably dominated by cosmic variance.

The implications of the above results are illustrated in Figure 18, where we show the fading rate $\Delta^{0.55}M_i/\Delta z$ for a set of single stellar population models, as a function of the age at $z = 0.70$. In particular, we show both FSPS models (solid lines) and the Maraston et al. (2009) passive LRG model (M09, crosses). Let us first focus on the FSPS models; we show models for three different metallicities and with or without a moderate amount of dust. The fading rate is clearly an excellent tracer of the age of a stellar population (under the SSP assumption) because it allows us to break the model degeneracy. If we assume SSP τ -models, a fading rate of 1.18 mag per unit redshift (passive model) at $z \sim 0.55$ would be consistent with a formation time for the LRGs of ~ 5 Gyr at $z = 0.70$ (there is actually a range of ages consistent with this fading rate, i.e. $\sim 4 - 5$ Gyr). This implies a formation redshift of $z = 2.0 - 3.0$.

Equal conclusions regarding the age of the LRG population are drawn when comparing our results with the M09 model, as Figure 18 shows. Maraston et al. (2009) were able to match the observed g, r, i colors of the LRG population across the redshift range $0.1 < z < 0.7$. In order to achieve this goal, the model requires ~ 3 per cent of the stellar mass to be in old metal-poor stars. Maraston et al. (2009) also show that empirical stellar libraries such as the Pickles library (Pickles 1998) provide considerably better fits than theoretical libraries. The FSPS grid used here and the M09 model provide similar predictions for the later evolutionary stages (> 3 Gyr) of an SSP, as far as the fading rate is concerned. Below ~ 3 Gyr models diverge considerably, although this is the range where stellar populations evolve rapidly, so relatively small differences in the models can translate into large differences in the fading rate.

An SSP assumes by definition that star formation takes place instantaneously. For an exponentially decaying model this implies that the e-folding time of the SFH, τ , is equal to 0. Figure 19 shows the effect of increasing τ on the fading rate of a set of CSP models. Each solid line represents a model with no dust, solar metallicity and a particular value for τ , ranging between $\tau \sim 0$ Gyr and $\tau = 3.38$ Gyr. The

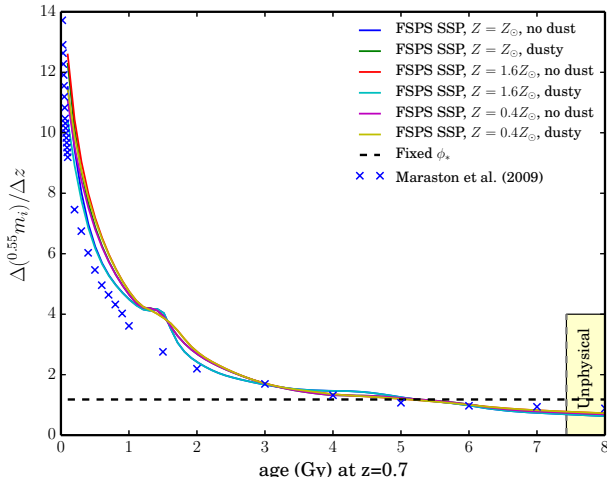


Figure 18. The fading rate $\Delta^{0.55} m_i / \Delta z$ for a set of SSPs as a function of the age at $z = 0.70$. Solid lines represent FSPS models covering a wide range of stellar population parameters and crosses show the M09 passive LRG model. The black dashed line represents a fading rate of 1.18 mag per unit redshift. These value corresponds to the fading rate within the redshift range $0.525 \leq z \leq 0.650$ for the best-fit passive-evolving fixed- Φ_* model.

corresponding shaded regions represent the variation within the same parameter space shown previously in Figure 18. When $\tau \ll 1$ Gyr, CSP models correspond basically to SSPs. As τ increases, the formation time of the population is pushed back for a constant fading rate. However, for sufficiently high fading rates ($\gtrsim 1.5$), the formation time reaches a maximum, towards early times, then moves back to later cosmological times (as τ increases). In essence, when $\tau < 1$ Gyr the SFR has enough time to decay so the change in the fading rate is due to the passive dimming of the stellar populations. Depending on the fading rate, there is a value of τ at which the SF is sufficiently active to start flattening the dimming rate. A value of $\Delta^{0.55} M_i / \Delta z = 1.18$ mag per unit redshift for the passive model can be consistent with a range of ages greater than ~ 5 Gyr up to that of the Big Bang, depending on the time scale for the SF.

6.6 The color evolution of the high-mass end of the red sequence

The unprecedented size of the CMASS sample allows us to compute the intrinsic colors of the RS as a function of redshift with remarkable accuracy. These results add important constraints to the stellar population properties of the LRGs (which are independent from our fading rate results). However, as previously pointed out, correcting for contamination from BC objects as a function of redshift causes a visible discontinuity in the RS colors at $z \simeq 0.60$. We must keep this issue in mind when analyzing the computed color evolution of the bright end of the red sequence and, in particular, when comparing with SPS models.

Before we discuss the colors predicted by the models, it is necessary to emphasize an important distinction between

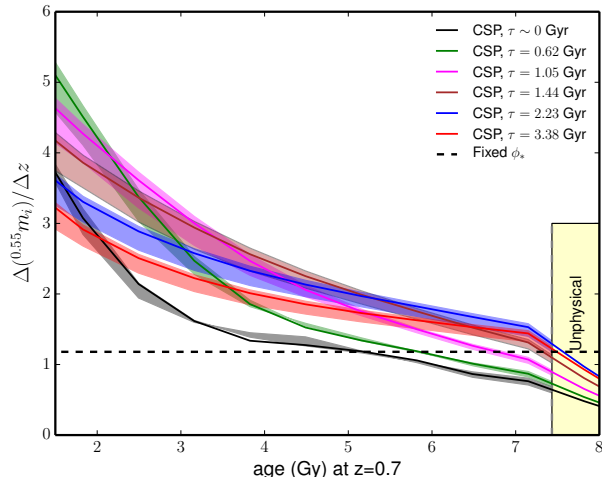


Figure 19. The same as Figure 18 but using CSP models with varying SFH e-folding time τ . Each solid line represents a model with no dust, solar metallicity and a particular value for τ , between $\tau \sim 0$ Gyr and $\tau = 3.38$ Gyr. The corresponding shaded regions encompass the same parameter space shown previously in Figure 18.

the FSPS and the M09 models used here. The FSPS grid that we built cover a wide range of metallicities, dust content and ages, providing a good coverage for the observed CMASS color-color distributions (as shown in Figure 6; recall the large photometric scatter along the g-r axis). The M09 model, on the other hand, is the result of a comprehensive stellar population fitting analysis specifically aimed at matching the observed colors of the LRG population as a function of redshift (as described in Maraston et al. 2009). Our conclusions regarding the FSPS models must, therefore, be restricted to the particular set of models that we use.

Figures 20 and 21 compare the computed $g - i$ color of the RS as a function of redshift with different sets of FSPS models. In particular, we focus on SSP models - Figures 20 - and, to illustrate the effect of τ , CSP models with $\tau = 0.75$ Gyr - Figure 21. In each figure, panels on the left-hand side correspond to models with no dust; panels on the right-hand side are models with a moderate amount of dust. Metallicity increases for panels from top to bottom ($Z = 0.40 Z_\odot, 0.63 Z_\odot, Z_\odot, 1.6 Z_\odot$). Each panel contains models of formation times at 2, 3, 4, 5, 6 and 7 Gy before $z = 0.7$, respectively.

It is well known that stellar population parameters are extremely degenerate, as far as the effect on the galaxy colors is concerned. Even though the computed $g - r$ and $r - i$ colors of the RS place some important constraints on the average SED of the RS, the implications for their stellar populations depend on a number of assumptions. Generally speaking, increasing metallicity or the amount of dust makes the colors redder. Conversely, increasing τ means increasing SF, which tends to make the colors bluer.

The first item to notice from Figure 20 is that the computed redshift evolution of the $g - i$ color seems too strong as compared to the models, at least under a single-age assump-

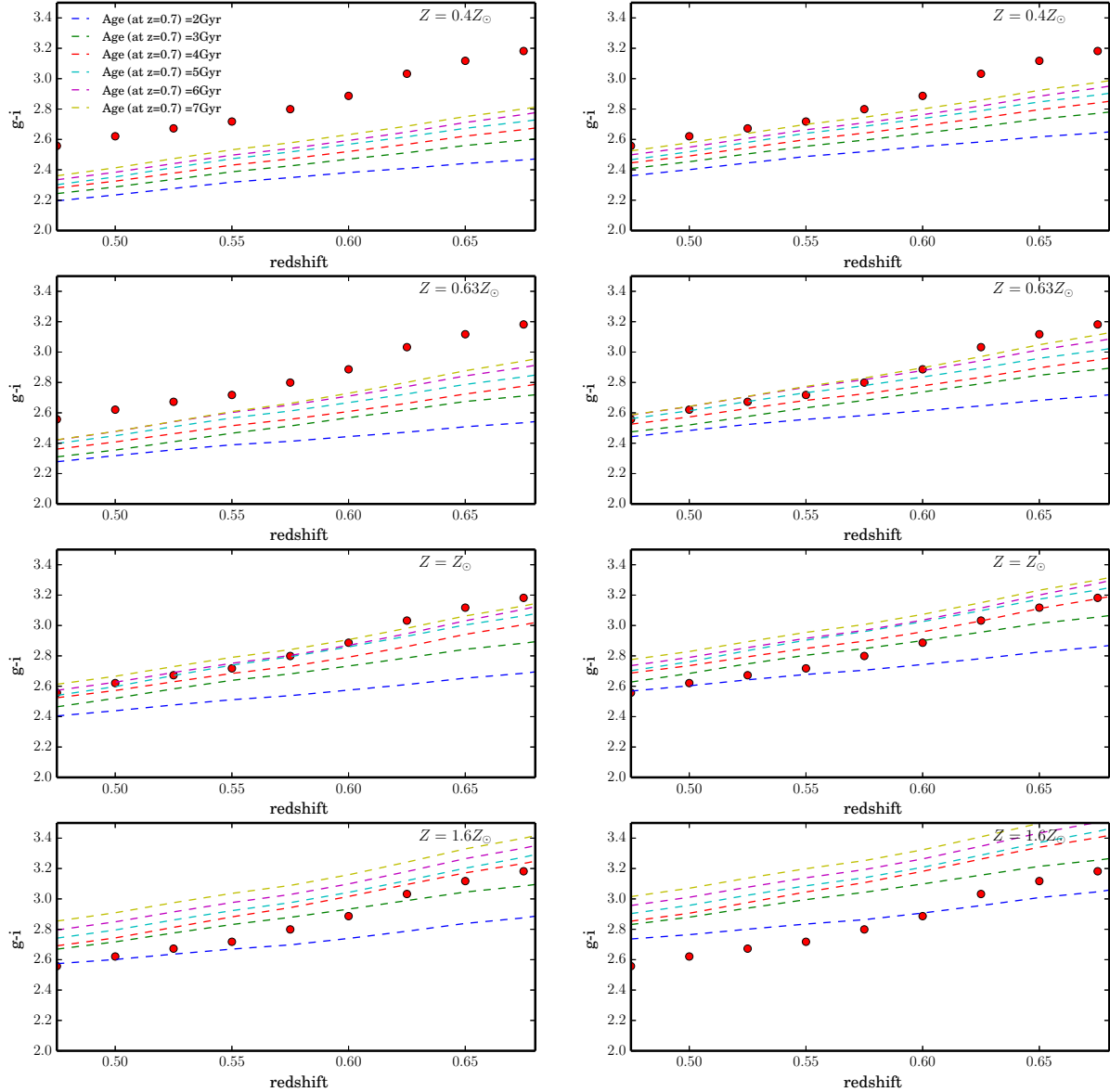


Figure 20. The redshift evolution of the $(g-i)$ centroid of the red sequence in intrinsic space, obtained using our fiducial model. Due to the magnitude dependence of the centroid, we show the value at the reference magnitude $i = 19.5 (Y_0 + Z_0)$. In each panel, the evolution of this color is compared with a set of SSP models, corresponding to 6 different formation times. In particular we plot the redshift evolution of the $g-i$ color for FSPS models formed 2,3,4,5,6 and 7 Gy before $z = 0.7$, respectively. The left-hand column corresponds to models without dust and the right-hand column to models with a moderate amount of dust. Finally, each row corresponds to a different metallicity, i.e. $Z = 0.40Z_\odot, 0.63Z_\odot, Z_\odot, 1.6Z_\odot$.

tion. This behaviour could be at least partially due to the discontinuity in the best-fit parameters at $z \simeq 0.60$. Given that the slope of the color-redshift relation appears to increase in the models, and assuming that correcting for the color discontinuity is unlikely to change the slope dramatically, our results seem to suggest rather old ages, of at least 5 Gyr at $z = 0.70$. In fact, if we make the plausible assumption that the LRGs are typically solar or super-solar metallicity

(last two rows in the Figures), the best agreement is to be found with solar-metallicity, dust-free models.

Increasing the SFH e-folding time τ varies the color-redshift trends for the models in a non-trivial way. When we increase the SFH e-folding time to $\tau \gtrsim 1$ the color trends get flattened considerably, what makes them rather inconsistent with our results. As we can see in Figure 21, an intermediate value for τ , i.e. $\tau \simeq 0.75$ Gyr, seems to provide the best agreement, as long as we restrict ourselves to the

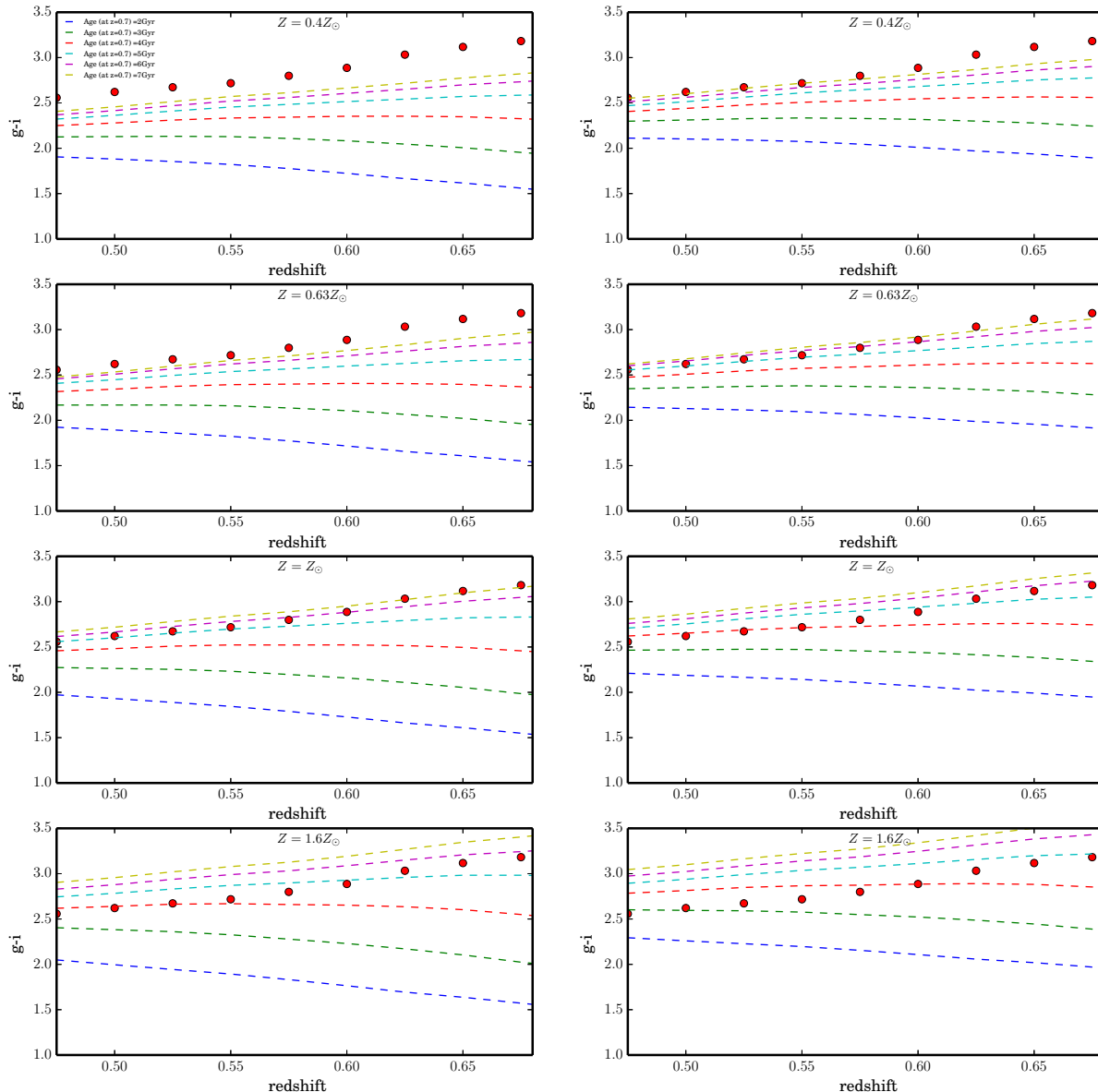


Figure 21. The redshift evolution of the $(g-i)$ centroid of the red sequence in intrinsic space, obtained using our fiducial model, as compared with FSPS CSP models with SHF e-folding time $\tau = 0.75$ Gyr. Due to the magnitude dependence of the centroid, we show the value at the reference magnitude $i = 19.5$ ($Y_0 + Z_0$). In each panel, the evolution of this color is compared with a set of SSP models, corresponding to 6 different formation times. In particular we plot the redshift evolution of the $g - i$ color for FSPS models formed 2,3,4,5,6 and 7 Gy before $z = 0.7$, respectively. The left-hand column corresponds to models without dust and the right-hand column to models with a moderate amount of dust. Finally, each row corresponds to a different metallicity, i.e $Z = 0.40Z_\odot, 0.63Z_\odot, Z_\odot, 1.6Z_\odot$.

no-dust, solar-metallicity case. This, again, seems to suggest a formation time of at least 5 Gyr before $z = 0.70$.

We have shown that the model degeneracy and the uncertainty on the determination of the location of the RS centroid in the color-color plane make it difficult to draw strong conclusions using the FSPS grid, as far as the color evolution is concerned. The M09 passive LRG model (Maraston et al. 2009), on the other hand, is known to match the observed g, r, i colors of the LRG population within the redshift range

$0.1 < z < 0.7$, so it should provide, by definition, tight constraints on the age of the LRG population. This fact is demonstrated in Figure 22, where the redshift evolution of the intrinsic RS $g-i$ color is compared with the M09 model, as a function of redshift. The RS colors agree almost perfectly with the colors predicted by the M09 model of 3 Gyr of age (at $z = 0.70$) for $z \lesssim 0.6$ and with the M09 model of 4 Gyr for $z \gtrsim 0.6$. As the color discontinuity that we obtain from our deconvolution method is most likely to be an artefact,

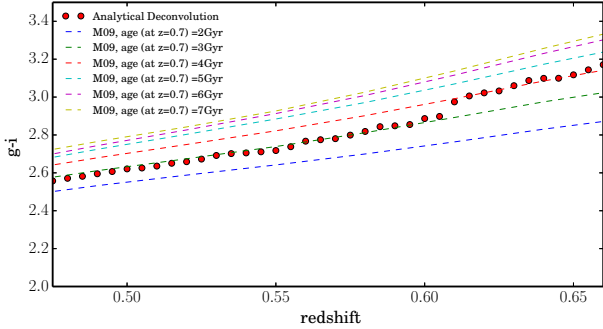


Figure 22. The redshift evolution of the $(g-i)$ centroid of the red sequence in intrinsic space, obtained using our fiducial model, as compared with the M09 model. Due to the magnitude dependence of the centroid, we show the value at the reference magnitude $i = 19.5$ ($Y_0 + Z_0$).

the values of 3 Gyr and 4 Gyr can be considered the lower and upper limits for a range of ages consistent with the data, respectively. Reducing the uncertainty on the determination of the RS color centroid and, consequently, on the inferred ages of the LRG population will certainly require the inclusion of spectroscopic data. The 3-4 Gyr age range inferred from the colors using the M09 models appears to be in some degree of tension with the 4-5 Gyr range inferred from the fading rate.

7 CONCLUSIONS AND FUTURE APPLICATIONS

The selection of the BOSS CMASS sample was designed to isolate the bright end ($17.5 < i < 19.9$) of the red sequence within the redshift range $0.45 \leq z \leq 0.70$, but also to include a fraction of bluer objects that increases with redshift. The observed CMASS color-color-magnitude distributions are, however, severely affected by photometric errors (especially along the $g-r$ axis). We have developed an analytical method based on an unbinned maximum likelihood approach for deconvolving the observed CMASS distributions from photometric blurring and accounting for selection effects. This method allows us to: (1) determine the best-fit intrinsic $(g-r)$ color- $(r-i)$ color- i -band magnitude distribution for the red sequence at intermediate redshifts with unprecedented accuracy, including a correction for the contamination from blue cloud objects in the sample; (2) determine red sequence completeness in the sample as a function of colors and magnitudes; (3) compute the bright end ($L \gtrsim 2L_*$) of the RS LF and its evolution with redshift.

Our results indicate that the red sequence at $z \sim 0.55$ is consistent with a single point on the color-color plane, which implies that the majority of the scatter observed in the CMASS distributions is due to photometric blurring. In order to fit the number counts, our model requires, however, a color-magnitude relation for the red sequence, with a slope of ≤ 0.05 mag per unit mag. The blue cloud, on the other hand, is well described by an extended Gaussian function

on the color-color plane, centered at $g-i \simeq 1.7$. Interestingly, the blue cloud intrinsically extends through the red side, which is consistent with the presence of red late-type galaxies. We estimate that the fraction of intrinsically blue cloud objects on the red side of the color-color diagram is $\sim 25-30\%$. The total fraction of intrinsically BC objects in the sample is 37%.

The fact that the CMASS sample is comprised of a remarkable fraction of non-early-type galaxies is in agreement with results from Masters et al. (2011), who studied the morphology of 240 BOSS galaxies at $0.3 < z < 0.7$ using both HST imaging and COSMOS data. Prior to the aforementioned study, Masters et al. (2010a) had found that red spirals constituted a significant fraction of all massive ($M \gtrsim 10^{10} M_\odot$) spirals found by the Galaxy Zoo project (Lintott et al. 2008), which suggests that massive galaxies are typically red, independently of their morphology. Quantitatively, however, notable discrepancies exist between our results and those from Masters et al. (2011). In particular, Masters et al. (2011) find that 29% of the CMASS galaxies in their 240-object sample did not present an early-type morphology; the majority are identified as late-type galaxies. Interestingly, only $\sim 10\%$ of these objects lie on the red side of the $g-i = 2.35$ demarcation, what would suggest a much more concentrated color distribution for the BC, as compared to our model. Additional investigation will be required to address these discrepancies, which could be simply due to the small size of the Masters et al. (2011) sample. Uncertainties associated with mapping observed colors to morphologies are also well documented, so a 10–20% scatter in such a relationship seems plausible.

Although our model fits well the observations, the possibility remains that an alternative model for the RS with a smoother transition towards the BC (such as a delta function plus a more extended Gaussian) provides even a better fit. This model could in principle alter the BC fraction. There is, unfortunately, only so much resolution that can be attained using photometric data, so the inclusion of spectroscopic data into the modeling should alleviate this tension. From a broader perspective, this aspect of the modeling, i.e., the connection between the RS and the BC and the role of the so-called *green valley* region in between, is key to understanding the way galaxies evolve (see examples of studies discussing these topics in Bundy et al. 2010 and Wolf et al. 2009).

As far as red sequence completeness is concerned, the sample is complete below $i \simeq 19.5$, where completeness starts to decline, depending on the redshift slice considered. Total completeness for the RS remains above $\sim 0.8-0.85$ at $z \gtrsim 0.53$. Below this redshift RS completeness drops rapidly due to the effect of the d_\perp cut. In order to minimize the effect of incompleteness and small magnitude coverage, we have computed the high-mass end of the RS LF within the redshift range $0.52 \leq z \leq 0.65$. Our results within the approximate absolute magnitude range $^{0.55}M_i \lesssim -22$ are, to a high level of confidence, consistent with the evolution of a Schechter function of $\Phi_* = (6.693 \pm 0.042) \times 10^{-4} \text{ Mpc}^{-3} \text{ mag}^{-1}$ passively fading by ~ 0.15 mag within the redshift range considered. Such fading rate measured at $z \sim 0.55$ cor-

responds to 1.18 mag per unit redshift. The strong evidence for passive evolution obtained from our accurate LF modeling confirms previous indications reported by independent groups using SDSS/BOSS data. Cool et al. (2008) reports an evolution of only 0.03 mag from $z = 1$ to $z = 0$ after correcting for passive evolution; although it must be kept in mind that the high-redshift sample ($0.6 < z < 1$) is only comprised by 300 galaxies. According to Cool et al. (2008), the evolution in the average LRG spectrum also supports a purely passive evolution for the LRGs since $z \sim 0.9$. This idea is reinforced by subsequent work from Maraston et al. (2013), who adopted a refined version of the LRG passive template used in Cool et al. (2008) - described in Maraston et al. 2009 -, to perform broad-band SED fitting on red galaxies from the BOSS DR9 dataset. Maraston et al. (2013) conclude that this template provides a good fit to BOSS galaxies redder than $g - i = 2.35$ at $0.4 < z < 0.7$. This template is also assumed in the computation of the stellar mass function in Maraston et al. (2013), which barely evolves within the redshift range considered. The results from Maraston et al. (2013), obtained with a large sample of galaxies, are extremely valuable, but they are subject to an adequate treatment of incompleteness in the BOSS samples. Finally, Tojeiro et al. (2012) develop a method for identifying the progenitors of SDSS I/II LRGs within the BOSS sample. They conclude that the LRG population at $z < 0.7$ evolves slowly, i.e., less than 2 per cent by merging, when the two samples are properly matched and weighted.

Even though our results are consistent with the aforementioned picture, we detect a small deviation from passive evolution towards brighter magnitudes. At the very-bright end (number density $\log_{10} \Phi = -6$), the RS LF has faded by ~ 0.07 mag more than the fainter galaxies (number density $\log_{10} \Phi = -4.5$). This result appears in disagreement with the common belief that the most massive early type galaxies form the stars faster than the less massive ones (downsizing). However, the deviation is small enough to prevent us from drawing any further conclusions. Recall that $\log_{10} \Phi = -6$ corresponds to mass range where we are completely dominated by cosmic variance.

When compared with single stellar population models, a fading rate of $\Delta^{0.55} M_i / \Delta z = 1.18$ mag per unit redshift is consistent with an age at $z = 0.7$ of $\sim 4 - 5$ Gyr, or, equivalently, a formation redshift of $z = 2.0 - 3.0$; both FSPS models and the M09 model provide similar predictions. Under the SSP assumption, the fading rate becomes an excellent tracer of the age of a stellar population, as the main parameter that drives the luminosity evolution of a stellar population is the age (thus it can be used to break the model degeneracy). When we allow for non-instantaneous star formation to occur (increasing τ), the formation redshift is pushed back to earlier cosmic times (using FSPS models). The typical formation redshift of a CSP with $\tau \sim 1$ Gyr and a fading rate of 1.18 mag per unit redshift is $z \simeq 6$, i.e., ≤ 1 Gyr after the Big Bang.

The intrinsic (non K-corrected) color of the RS reddens from $g - i \simeq 2.5$ at $z \simeq 0.50$ to $g - i \simeq 3.2$ at $z \simeq 0.70$ (at $i \simeq 19.5$, note the color-magnitude relation). The accuracy in the determination of the color centroid of the RS

is, to a certain extent, affected by the combined effect of the d_{\perp} cut and the limited resolution that can be attained using photometric data alone. The result of these effects on our deconvolution procedure is a discontinuity (jump) in the color-redshift trend at $z \simeq 0.60$ (of $\lesssim 0.1$ mag in the g-i color). Although this fact should be kept in mind, the following conclusions can be drawn when comparing the color-redshift trend with the predictions from stellar population models:

- From a simple comparison (no SPS fitting performed), it appears that the color evolution seems to be somehow consistent with solar-metallicity dust-free FSPS models with ages greater than ~ 5 Gyr (formation redshift of $z = 3$). This would be in agreement with our fading rate results. We note, however, a general discrepancy between the data and the models contained in our FSPS grid, so that the latter tend to predict milder evolutions. This discrepancy is somehow alleviated, for the older models, when we increase τ to ~ 0.75 Gyr. Importantly, the possibility remains that a different set of choices for the stellar population parameters of the FSPS models can mitigate or even eliminate these discrepancies.

- The M09 passive LRG model provides an excellent match to the intrinsic g,r,i colors of the LRG population. Our color measurements, given the discontinuity mentioned above, are consistent with a range of ages from 3 Gyr to 4 Gyr (at $z = 0.70$), which imply formation redshifts of $z = 1.5 - 2.0$. This 3-4 Gyr age range appears to be in some degree of tension with the 4-5 Gyr range inferred from the fading rate measurements.

We expect the results of this work to be immediately applicable to a number of future studies. First, in combination with the velocity-dispersion function measurement techniques of Shu et al. (2012), our LF and selection-function results will permit a determination of the relationship between stellar mass and velocity dispersion (e.g., Faber & Jackson 1976) at $z = 0.5$ for the most massive galaxies, including the intrinsic scatter in velocity dispersion at fixed stellar mass. Second, our results, in combination with the techniques of halo occupation distributions (HOD: e.g., Berlind & Weinberg 2002; Zehavi et al. 2005) and halo abundance matching (HAM: e.g., Vale & Ostriker 2004; Trujillo-Gomez et al. 2011), will permit more accurate quantitative analysis of galaxy clustering statistics and of the relationship between galaxies and dark-matter halos. Third, our redshift-dependent luminosity function can provide informative priors for the determination of spectroscopic redshifts from low signal-to-noise survey data in future enhancements to the redshift measurement pipeline for BOSS and subsequent surveys (Bolton et al. 2012). Fourth, we may use our red+blue photometric population model to deconvolve average spectra of red and blue galaxies within the BOSS sample. Finally, the forward-modeling techniques developed in this work can be applied to quantify the evolution of massive galaxies as a single population across redshift from $z \approx 1$ down to $z = 0$ by including other galaxy samples from SDSS-I, -II, -III, and -IV.

ACKNOWLEDGMENTS

This material is based upon work supported by the U.S. Department of Energy, Office of Science, Office of High Energy Physics, under Award Number DE-SC0010331.

The support and resources from the Center for High Performance Computing at the University of Utah are gratefully acknowledged.

AMD, FP, JC, CC, GF, SR thank the support from the Spanish MICINN's Consolider-Ingenio 2010 Programme under grant MultiDark CSD2009-00064, AYA2010-21231-C02-01, and MINECO Centro de Excelencia Severo Ochoa Programme under grant SEV-2012-0249.

Funding for SDSS-III has been provided by the Alfred P. Sloan Foundation, the Participating Institutions, the National Science Foundation, and the U.S. Department of Energy Office of Science. The SDSS-III Web site is <http://www.sdss3.org/>.

SDSS-III is managed by the Astrophysical Research Consortium for the Participating Institutions of the SDSS-III Collaboration including the University of Arizona, the Brazilian Participation Group, Brookhaven National Laboratory, University of Cambridge, University of Florida, the French Participation Group, the German Participation Group, the Instituto de Astrofísica de Canarias, the Michigan State/Notre Dame/JINA Participation Group, Johns Hopkins University, Lawrence Berkeley National Laboratory, Max Planck Institute for Astrophysics, New Mexico State University, New York University, Ohio State University, Pennsylvania State University, University of Portsmouth, Princeton University, the Spanish Participation Group, University of Tokyo, The University of Utah, Vanderbilt University, University of Virginia, University of Washington, and Yale University.

REFERENCES

- Abazajian K. N., Adelman-McCarthy J. K., Agüeros M. A., et al., 2009, *ApJS*, 182, 543
- Ahn C. P., Alexandroff R., Allende Prieto C., et al., 2012, *ApJS*, 203, 21
- Ahn C. P., Alexandroff R., Allende Prieto C., et al., 2013, *ArXiv e-prints*
- Aihara H., Allende Prieto C., An D., et al., 2011, *ApJS*, 193, 29
- Anderson L., Aubourg É., Bailey S., et al., 2014, *MNRAS*, 441, 24
- Balogh M. L., Miller C., Nichol R., Zabludoff A., Goto T., 2005, *MNRAS*, 360, 587
- Bell E. F., Wolf C., Meisenheimer K., et al., 2004, *ApJ*, 608, 752
- Berlind A. A., Weinberg D. H., 2002, *ApJ*, 575, 587
- Bernardi M., Nichol R. C., Sheth R. K., Miller C. J., Brinkmann J., 2006, *AJ*, 131, 1288
- Blanton M. R., Dalcanton J., Eisenstein D., et al., 2001, *AJ*, 121, 2358
- Blanton M. R., Lin H., Lupton R. H., et al., 2003, *AJ*, 125, 2276
- Blumenthal G. R., Faber S. M., Primack J. R., Rees M. J., 1984, *Nature*, 311, 517
- Bolton A. S., Schlegel D. J., Aubourg É., et al., 2012, *AJ*, 144, 144
- Bower R. G., Lucey J. R., Ellis R. S., 1992, *MNRAS*, 254, 589
- Brough S., Collins C. A., Burke D. J., Mann R. G., Lynam P. D., 2002, *MNRAS*, 329, L53
- Bundy K., Scarlata C., Carollo C. M., et al., 2010, *ApJ*, 719, 1969
- Clemens M. S., Bressan A., Nikolic B., Alexander P., Annibali F., Rampazzo R., 2006, *MNRAS*, 370, 702
- Clemens M. S., Bressan A., Nikolic B., Rampazzo R., 2009, *MNRAS*, 392, L35
- Coil A. L., Blanton M. R., Burles S. M., et al., 2011, *ApJ*, 741, 8
- Colless M., Dalton G., Maddox S., et al., 2001, *MNRAS*, 328, 1039
- Conroy C., Gunn J. E., White M., 2009, *ApJ*, 699, 486
- Cool R. J., Eisenstein D. J., Fan X., et al., 2008, *ApJ*, 682, 919
- Cool R. J., Moustakas J., Blanton M. R., et al., 2013, *ApJ*, 767, 118
- Croton D. J., Springel V., White S. D. M., et al., 2006, *MNRAS*, 365, 11
- Dawson K. S., Schlegel D. J., Ahn C. P., et al., 2013, *AJ*, 145, 10
- de Propris R., Stanford S. A., Eisenhardt P. R., Dickinson M., Elston R., 1999, *AJ*, 118, 719
- Eisenstein D. J., Annis J., Gunn J. E., et al., 2001, *AJ*, 122, 2267
- Eisenstein D. J., Weinberg D. H., Agol E., et al., 2011, *AJ*, 142, 72
- Eisenstein D. J., Zehavi I., Hogg D. W., et al., 2005, *ApJ*, 633, 560
- Ellis R. S., Smail I., Dressler A., et al., 1997, *ApJ*, 483, 582
- Faber S. M., Jackson R. E., 1976, *ApJ*, 204, 668
- Faber S. M., Willmer C. N. A., Wolf C., et al., 2007, *ApJ*, 665, 265
- Falco E. E., Kurtz M. J., Geller M. J., et al., 1999, *PASP*, 111, 438
- Frieman J. A., Bassett B., Becker A., et al., 2008, *AJ*, 135, 338
- Fukugita M., Ichikawa T., Gunn J. E., Doi M., Shimasaku K., Schneider D. P., 1996, *AJ*, 111, 1748
- Glazebrook K., Abraham R. G., McCarthy P. J., et al., 2004, *Nature*, 430, 181
- Gunn J. E., Carr M., Rockosi C., et al., 1998, *AJ*, 116, 3040
- Gunn J. E., Siegmund W. A., Mannery E. J., et al., 2006, *AJ*, 131, 2332
- Holden B. P., Blakeslee J. P., Postman M., et al., 2005, *ApJ*, 626, 809
- Huchra J., Davis M., Latham D., Tonry J., 1983, *ApJS*, 52, 89
- Jimenez R., Bernardi M., Haiman Z., Panter B., Heavens A. F., 2007, *ApJ*, 669, 947
- Kauffmann G., White S. D. M., Guiderdoni B., 1993, *MNRAS*, 264, 201
- Kauffmann G., White S. D. M., Heckman T. M., et al.,

- 2004, MNRAS, 353, 713
- Kodama T., Arimoto N., Barger A. J., Aragón-Salamanca A., 1998, A&A, 334, 99
- Komatsu E., Smith K. M., Dunkley J., et al., 2011, ApJS, 192, 18
- Lin H., Kirshner R. P., Shectman S. A., et al., 1996, ApJ, 464, 60
- Lintott C. J., Schawinski K., Slosar A., et al., 2008, MNRAS, 389, 1179
- Loveday J., 1997, ApJ, 489, 29
- Maraston C., Pforr J., Henriques B. M., et al., 2013, MNRAS, 435, 2764
- Maraston C., Strömbäck G., Thomas D., Wake D. A., Nichol R. C., 2009, MNRAS, 394, L107
- Marzke R. O., Huchra J. P., Geller M. J., 1994, ApJ, 428, 43
- Masters K. L., Maraston C., Nichol R. C., et al., 2011, MNRAS, 418, 1055
- Masters K. L., Mosleh M., Romer A. K., et al., 2010a, MNRAS, 405, 783
- Masters K. L., Nichol R., Bamford S., et al., 2010b, MNRAS, 404, 792
- McCarthy P. J., Le Borgne D., Crampton D., et al., 2004, ApJL, 614, L9
- Montero-Dorta A. D., Prada F., 2009, MNRAS, 399, 1106
- Newman J. A., Cooper M. C., Davis M., et al., 2013, ApJS, 208, 5
- Norberg P., Cole S., Baugh C. M., et al., 2002, MNRAS, 336, 907
- Oke J. B., Gunn J. E., 1983, ApJ, 266, 713
- Pickles A. J., 1998, PASP, 110, 863
- Richards G. T., Strauss M. A., Fan X., et al., 2006, AJ, 131, 2766
- Schawinski K., Kaviraj S., Khochfar S., et al., 2007, ApJS, 173, 512
- Schechter P., 1976, ApJ, 203, 297
- Schlegel D., White M., Eisenstein D., 2009, in astro2010: The Astronomy and Astrophysics Decadal Survey, vol. 2010 of ArXiv Astrophysics e-prints, 314+
- Shectman S. A., Landy S. D., Oemler A., et al., 1996, ApJ, 470, 172
- Shu Y., Bolton A. S., Schlegel D. J., et al., 2012, AJ, 143, 90
- Smee S. A., Gunn J. E., Uomoto A., et al., 2013, AJ, 146, 32
- Somerville R. S., Primack J. R., 1999, MNRAS, 310, 1087
- Springel V., White S. D. M., Jenkins A., et al., 2005, Nature, 435, 629
- Stoughton C., Lupton R. H., Bernardi M., et al., 2002, AJ, 123, 485
- Strateva I., Ivezić Ž., Knapp G. R., et al., 2001, AJ, 122, 1861
- Strauss M. A., Weinberg D. H., Lupton R. H., et al., 2002, AJ, 124, 1810
- Thomas D., Maraston C., Bender R., Mendes de Oliveira C., 2005, ApJ, 621, 673
- Thomas D., Maraston C., Schawinski K., Sarzi M., Silk J., 2010, MNRAS, 404, 1775
- Tojeiro R., Percival W. J., Wake D. A., et al., 2012, MNRAS, 424, 136
- Trujillo-Gomez S., Klypin A., Primack J., Romanowsky A. J., 2011, ApJ, 742, 16
- Vale A., Ostriker J. P., 2004, MNRAS, 353, 189
- Wake D. A., Collins C. A., Nichol R. C., Jones L. R., Burke D. J., 2005, ApJ, 627, 186
- White S. D. M., Frenk C. S., 1991, ApJ, 379, 52
- White S. D. M., Rees M. J., 1978, MNRAS, 183, 341
- Willmer C. N. A., Faber S. M., Koo D. C., et al., 2006, ApJ, 647, 853
- Wolf C., Aragón-Salamanca A., Balogh M., et al., 2009, MNRAS, 393, 1302
- Wolf C., Meisenheimer K., Rix H., Borch A., Dye S., Kleinheinrich M., 2003, A&A, 401, 73
- York D. G., Adelman J., Anderson Jr. J. E., et al., 2000, AJ, 120, 1579
- Zehavi I., Zheng Z., Weinberg D. H., et al., 2005, ApJ, 630, 1